Journal of Inorganic Biochemistry 199 (2019) 110792

Contents lists available at ScienceDirect

Journal of Inorganic Biochemistry

journal homepage: www.elsevier.com/locate/jinorgbio

A palladium(II) complex with the Schiff base 4-chloro-2-(*N*-ethyliminomethyl)-phenol: Synthesis, structural characterization, and *in vitro* and *in silico* biological activity studies

Ariadni Zianna[a,*], George D. Geromichalos[a,*], Anna Pekou[b], Antonios G. Hatzidimitriou[a], Evdoxia Coutouli-Argyropoulou[c], Maria Lalia-Kantouri[a], Anastasia A. Pantazaki[b,*], George Psomas[a,*]

[a] *Laboratory of Inorganic Chemistry, Department of Chemistry, Aristotle University of Thessaloniki, Thessaloniki GR-54124, Greece*
[b] *Laboratory of Biochemistry, Department of Chemistry, Aristotle University of Thessaloniki, Thessaloniki GR-54124, Greece*
[c] *Laboratory of Organic Chemistry, Department of Chemistry, Aristotle University of Thessaloniki, Thessaloniki GR-54124, Greece*

ARTICLE INFO

Keywords:
Palladium(II) complex
Schiff base
DNA-interaction
Interaction with serum albumins
In silico molecular docking
In silico predictive tools

ABSTRACT

The synthesis and characterization of the Pd(II) complex of the formula $[Pd(L)_2]$ **1** with the Schiff base 4-chloro-2-(*N*-ethyliminomethyl)-phenol (HL) as derived *in situ via* the condensation reaction of 5-chloro-salicylaldehyde and ethylamine was undertaken. The structure of **1** was verified by single-crystal X-ray crystallography. The ability of **1** to interact with calf-thymus (CT) DNA was studied by UV–vis and viscosity experiments, and its ability to displace ethidium bromide (EB) from the DNA-EB conjugate was revealed by fluorescence spectroscopy. It was found that intercalation is the most possible mode of interaction with CT DNA. Additionally, DNA electrophoretic mobility experiments showed that **1** interacts with the plasmid **pBluescript SK**(+) (pDNA) as proved by the formation of unusual mobility DNA bands and degradation of relaxed pDNA at concentration of 5 mM. The interaction of **1** with human (HSA) and bovine serum albumin (BSA) was monitored revealing its reversible binding to albumins. The complex showed noteworthy antimicrobial activity against one (*Bacillus subtilis*) of the five tested bacteria. In order to explain the described *in vitro* activity of the compound, we adopted molecular docking studies on the crystal structure of HSA, BSA, CT DNA and DNA-gyrase. Furthermore, *in silico* predictive tools have been employed to study the properties of the complex. The *in silico* studies are adopted on a multitude of proteins involved in cancer growth, as well as prediction of drug-induced changes of gene expression profile, protein- and mRNA-based prediction results, prediction of sites of metabolism, cytotoxicity for cancer cell lines, *etc*.

1. Introduction

The interest concerning the synthesis of palladium complexes has been significantly increased recently because of their numerous potential applications in areas, such as catalysis, medicine and material science [1–4]. In the field of Bioinorganic Chemistry, palladium compounds have gained attention mainly due to their similarity regarding coordination modes with platinum compounds used as anticancer agents [4], although the Pd complexes seem to hydrolyze more rapidly [5]. Furthermore, many Pd complexes have been reported to exhibit *in vitro* anti-viral, anti-fungal, antimicrobial [6], anti-inflammatory [7], and antioxidant properties [8]. The ligands in these complexes are mainly N-, S- or P-donors, such as thiosemicarbazones, dithiocarbamates, thioamides, amines, and especially Schiff bases [6,9].

As known, Schiff bases are organic compounds containing an imine group ($-RC{=}N-$). They are usually prepared by the condensation reaction of a primary amine and a carbonyl compound (either aldehyde or ketone) [10,11]. They are at least bidentate N,O-donor ligands when coordinated to diverse metal ions. The Schiff bases and their metal complexes have shown a variety of activities [12], including catalytic [13] and biological (antibacterial [14], antibiofilm [15], antifungal [16], antimalarial [17], antioxidant [18], anticancer [19], antiviral [20]), properties (luminescence [21], fluorescence [22] and non-linear optical [23]) and potential applications (as in sensors [24] and

---

* Corresponding authors.

E-mail addresses: ariadnezianna@gmail.com (A. Zianna), gerom@chem.auth.gr (G.D. Geromichalos), natasa@chem.auth.gr (A.A. Pantazaki), gepsomas@chem.auth.gr (G. Psomas).

https://doi.org/10.1016/j.jinorgbio.2019.110792
Received 6 April 2019; Received in revised form 16 July 2019; Accepted 21 July 2019

photovoltaic materials [25]).

Considering the palladium(II) complexes with Schiff bases as ligands, a plethora of compounds has been reported; in many of them, the Schiff base ligand is a derivative of salicylaldehyde and is a bidentate N,O-donor [26–29]. The Pd(II)-Schiff base complexes have been examined for their catalytic activity [29–31] or have shown *in vitro* biological activity (antimicrobial [26,32], antifungal [27] and cytotoxic [28,33,34]).

Serum albumins (SAs) are the most abundant plasma proteins in mammals, playing a key-role in drug transportation. SAs are multifunctional proteins with extraordinary ligand-binding capacity, making them ideal transporter molecules for a diverse range of metabolites, drugs, nutrients, metals and other molecules. Due to their ligand-binding properties, SAs have wide clinical, pharmaceutical, and biochemical applications [35,36], since a wide variety of drugs are delivered to their targeting organs/tissues by binding with human serum albumin (HSA). Such studies are of great importance for pharmaceutical industry, not only because of the impact as an efficient drug-delivery system, but also for the ability of the albumin to modify the pharmacokinetic profile of drugs [37,38]. DNA is recognized as one of the most common biological targets of anticancer drugs, since one of the main mechanisms of action of the anticancer drugs is the damage of DNA [39]. Bacterial DNA-gyrase is a topoisomerase type II enzyme that has attracted attention since its discovery in 1976, when it was first isolated from *Escherichia coli* [40]. DNA-gyrase catalyzes changes in DNA-topology by breaking and rejoining double-stranded DNA, introducing negative supercoils of the closed-circular DNA in front of the replication fork [41]. As this function is essential for DNA-replication and transcription, DNA-gyrase is really a suitable target for antibacterial agents, since its blocking induces bacterial cell death.

As a continuation of our research concerning palladium(II) metal complexes with substituted salicylaldehydes (X-saloH, X = 3-OCH_3, 5-NO_2, 5-Cl or 5-Br) derivatives [42], we have isolated and characterized a palladium(II) complex with a Schiff base ligand (4-chloro-2-(*N*-ethyliminomethyl)-phenol, HL) derived from the condensation reaction of 5-chloro-salicylaldehyde and ethylamine. The resulting complex has the formula [Pd(4-chloro-2-(ethyliminomethyl)-phenolato-κ^2N,O)$_2$] ([Pd(L)$_2$], **1**) and its structure was verified by physicochemical and spectroscopic techniques (IR, UV–vis) as well as single-crystal X-ray crystallography. The calf-thymus (CT) DNA-binding mode of the complex was investigated by (i) UV–vis spectroscopy and the DNA-binding constants of the complex (K_b) were determined, (ii) DNA-viscosity measurements and (iii) competitive DNA-binding studies with the classic intercalator ethidium bromide (EB) investigated by fluorescence emission spectroscopy. Moreover, in order to visualize a possible interaction and the influence of complex **1** on the structure of plasmid **pBluescript SK**(+) (pDNA), electrophoretic mobility experiments were performed. The affinity of the complex for HSA and bovine serum albumin (BSA) was studied by fluorescence emission spectroscopy and the corresponding binding constants were determined. The antimicrobial activity of complex **1** was evaluated against five bacterial species: *Escherichia coli* XL1 (*E. coli*), *Xanthomonas campestris* ATCC 33013 (*X. campestris*), *Staphylococcus aureus* ATCC 29213 (*S. aureus*), *Bacillus subtilis* ATCC 6633 (*B. subtilis*) and *Bacillus cereus* ATCC 11778 (*B. cereus*). Furthermore, *in silico* studies adopting various procedures with the employment of molecular docking simulations on the crystal structure of CT DNA, DNA-gyrase and the target albumins HSA and BSA, were employed with the aim to explore the ability of complex **1** to bind to these macromolecules, contributing thus in the understanding of the role to act as antibacterial agent and suggesting a mode of action of compound **1**. Additionally, a variety of computational tools were employed to predict the complete biological activity profile of the synthesized complex **1**. Predictive tools include general pharmacological potential (prediction of activity spectra for substances (PASS)), prediction of target proteins affected by the compound, prediction of drug-induced changes of gene expression profile, protein and mRNA based prediction results, prediction substrate/metabolite specificity (SMP) and sites of metabolism (SOMP), prediction of cytotoxicity for tumor and non-tumor cell lines, rodent organ-specific carcinogenicity prediction (ROSC-Pred) and calculation of absorption, distribution, metabolism, excretion, and toxicity (ADMET) parameters, pharmacokinetic properties, druglike nature and medicinal chemistry friendliness of the compound. It is among the few cases that so many extensive *in vitro* and *in silico* studies of the biological activity of a Pd(II) complex with Schiff base ligands have been employed and reported.

2. Experimental

2.1. Materials - instrumentation - physical measurements

All chemical reagents used in the present study, *i.e.* 5-Cl-saloH, Pd(CH_3COOH)$_2$, ethylamine (EtNH_2), trisodium citrate, NaCl, CT DNA, EB, BSA and HSA were obtained as reagent grade from Sigma-Aldrich Co. and used as received. All solvents were obtained from Chemlab and were used without further purification.

The CT DNA stock solution was prepared by dilution of CT DNA to buffer (containing 150 mM NaCl and 15 mM trisodium citrate at pH 7.0) followed by exhaustive stirring at 4 °C for 3 days, and kept at 4 °C for no longer than ten days. The DNA concentration per nucleotide was determined by the UV absorbance at 260 nm after 1:20 dilution using $\varepsilon = 6600\ M^{-1}\ cm^{-1}$ [43]. The stock solution of CT DNA gave a ratio of UV absorbance at 260 and 280 nm (A_{260}/A_{280}) of 1.88, indicating that the DNA was sufficiently free of protein contamination [44].

Infrared (IR) spectra (400–4000 cm^{-1}) were recorded on a Nicolet FT-IR 6700 spectrometer with samples prepared as KBr pellets. UV–visible (UV–vis) spectra of the compounds as nujol mulls or in DMSO solution (in the range 1×10^{-5}–5×10^{-3} M) were recorded on a Hitachi U-2001 dual beam spectrophotometer. ^1H NMR spectra were recorded at 300 MHz on a Bruker AVANCE III 300 spectrometer using DMSO-d_6 as solvent. Mass spectra were determined on an LC-MS 2010 EV Instrument (Shimadzu) under electrospray ionization (ESI) conditions. C, H and N elemental analyses were performed on a PerkinElmer 240B elemental microanalyzer. Molecular conductivity measurements of 1 mM DMSO solution of the complexes were carried out with a Crison Basic 30 conductometer. Fluorescence spectra were recorded in solution on a Hitachi F-7000 fluorescence spectrophotometer. Viscosity experiments were carried out using an ALPHA L Fungilab rotational viscometer equipped with an 18 mL LCP spindle and the measurements were performed at 100 rpm.

2.2. Synthesis of the complex

The Schiff base HL was prepared *in situ* by the addition of ethylamine (1 mmol, 45 mg) into a CH_3CN solution (15 mL) of 5-Cl-saloH (1 mmol, 156 mg) which was stirred at room temperature for 30 min. A CH_3CN solution (15 mL) of Pd(CH_3COOH)$_2$ (0.5 mmol, 112 mg) was added to this solution and the resulting solution was stirred for additional 30 min and then turned into yellow. Orange-yellow crystals of complex [Pd(L)$_2$], **1** suitable for single-crystal X-ray structure determination (yield 42%, 198 mg) were formed after a few days. Anal. calc. $C_{18}H_{18}Cl_2N_2O_2Pd$ (MW = 471.6): C: 45.83, H: 3.85, N: 5.93%; found: C: 45.90, H: 3.85, N: 5.91%. ESI(+) MS in MeCN (*m/z*): found: 473, calcd. for $(\mathbf{1} + H)^+$: 472.6; found: 186, calcd for HL^+: 184; found: 156, calcd for 5-Cl-saloH: 156, IR spectrum (KBr), selected peaks (ν, in cm^{-1}): 1662 (strong) ν(C=N), 1308 (strong-to-medium) ν(C−O → Pd), 507 (medium) ν(Pd−O), 460 (medium) ν(Pd−N). UV–vis spectra: as nujol mull, λ/nm: 395, 450(shoulder (sh)); in DMSO, λ/nm (ε/$M^{-1}\ cm^{-1}$): 270 (18900), 397 (4900), 445(sh) (1500). ^1H NMR spectrum in DMSO-d_6 (δ/ppm) (the numbering of H atoms is shown in Scheme 1): 8.06 (2H, s, H^7), 7.43 (2H, d, *J* = 2.8 Hz, H^6), 7.23 (2H, dd, *J* = 9.0, 2.8 Hz, H^4), 6.77 (1H, d, *J* = 9.0 Hz, H^3), 3.83 (4H, q,

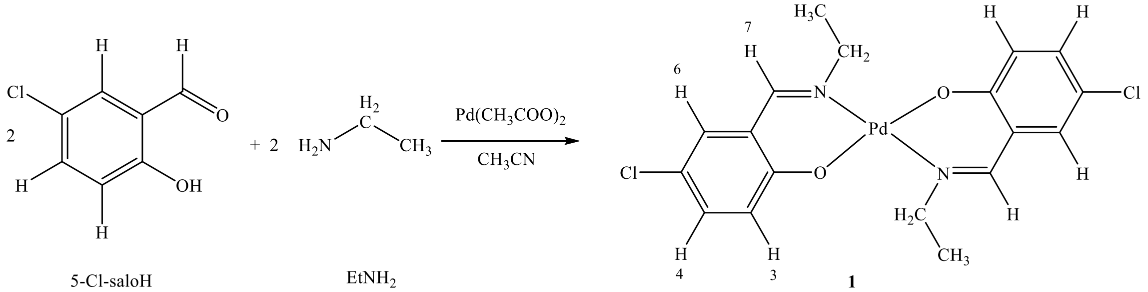

Scheme 1. Synthetic route for complex **1**. The numbering of H atoms in L^{-1} is also provided.

$J = 6.9$ Hz, $-CH_2-$), 1.25 (6H, t, $J = 6.9$ Hz, $-CH_3$). Λ_M (1 mM DMSO) = 7 mho·cm^2·mol^{-1}.

2.3. X-ray crystal structure determination

Single-crystals of complex **1** suitable for X-ray crystallography structure analysis were obtained by slow evaporation of the mother liquid at room temperature. A crystal of **1** was mounted at room temperature on a Bruker Kappa APEX2 diffractometer equipped with a triumph monochromator using Mo Kα radiation. Unit cell dimensions were determined and refined by using the angular settings of at least 191 high intensity reflections ($>10\ \sigma(I)$) in the range $11 < 2\theta\ \omega < 36°$. Intensity data were recorded using ϕ and ω scans. Crystal presented no decay during the data collection. The frames collected were integrated with the Bruker SAINT Software package [45], using a narrow-frame algorithm. Data were corrected for absorption using the numerical method (SADABS) based on crystal dimensions [46]. The structures was solved using the SUPERFLIP package [47], incorporated in Crystals. Data refinement (full-matrix least-squares methods on F^2) and all subsequent calculations were carried out using the Crystals version 14.61_build_6236 program package [48]. All non-hydrogen atoms were refined anisotropically. Hydrogen atoms were located by difference maps at their expected positions and refined using soft constraints. By the end of the refinement, they were positioned geometrically using riding constraints to bonded atoms. Illustration was drawn by CAMERON [49]. Crystallographic data for complex **1** are presented in Table S1.

2.4. In vitro biological activity studies

In order to study *in vitro* the biological activity of complex **1** (*i.e.*, antimicrobial activity and interaction with DNA or albumins), the complex is initially dissolved in DMSO (1 mM). Mixing of such solutions with the aqueous buffer DNA solutions used never exceeded 5% DMSO (v/v) in the final solution, which was needed due to low aqueous solubility of compound **1**.

The interaction of the complex with CT DNA was investigated by UV–vis spectroscopy and viscosity measurements and *via* the evaluation of its EB-displacing ability which was studied by fluorescence emission spectroscopy. The interaction of the complex with pDNA was monitored by agarose gel electrophoresis experiments. The albumin (BSA or HSA) binding studies were performed by tryptophan fluorescence quenching experiments. The antimicrobial activity of the complex was evaluated by determining the Half-Minimal Inhibitory Concentration (IC_{50}) values toward two Gram-(−) (*E. coli* and *X. campestris*) and three Gram-(+) (*S. aureus*, *B. cereus* and *B. subtilis*) bacterial species. Detailed procedures regarding the *in vitro* study of the biological activity of the complex are given in the Supporting information (Section S1).

2.5. In silico computational methods

A series of *in silico* calculations were employed in order to predict the biological activity of the complex. These studies include: (i) molecular modeling and docking calculations on the crystal structure of CT DNA dodecamer d(CpGpCpGpApApTpTpCpGpCpG), HSA, BSA and DNA-gyrase, (ii) plasma protein binding (PPB) for target prediction in ChEMB database, (iii) PASS, (iv) prediction of cytotoxicity for tumor and non-tumor cell lines *via* Cell Line Cytotoxicity Predictor (CLC-Pred), (v) drug-induced gene expression profiles prediction (DIGEP-Pred), (vi) SMP, (vii) SOMP, (viii) ROSC-Pred, (ix) prediction of toxicity of chemicals (ProTox-II) and oral rat toxicity prediction, (x) SwissTargetPrediction and (xi) ADMET (SwissADME prediction and ADMET structure-activity relationship server (admetSAR) prediction). Details concerning the *in silico* biological properties of the complex are given in the Supporting information (Section S2).

3. Results and discussion

3.1. Synthesis

The Schiff base HL was prepared *in situ via* the reaction of 5-Cl-saloH with $EtNH_2$ in CH_3CN. The addition of the Pd(II) salt in this solution in a 1:2 Pd:HL ratio resulted in the formation of complex **1** (Scheme 1).

The obtained palladium(II) complex **1** is neutral (the molar conductivity in DMSO solution was found 7 mho·cm^2·mol^{-1}) [50] and possesses a 1:2 Pd:L composition, as it has been indicated from elemental analyses. The ESI(+) mass spectrum of the complex (Fig. S1) was recorded in acetonitrile; the obtained molecular ion was found at *m/z* 473 which is satisfactorily close to the calculated value of 472.6. The complex can be well-dissolved in DMSO and DMF, but it is less soluble or insoluble in common organic solvents and water.

Evidence of the formation and the coordination mode of the ligand in complex **1** was also derived from the interpretation of the IR, ^1H NMR and UV–vis spectra, as well as by single-crystal X-ray crystallography analysis.

3.2. Crystal structure of complex 1

The molecular structure of complex $[Pd(L)_2]$, **1** was verified by X-Ray crystallography and is presented in Fig. 1.

Complex **1** is centrosymmetric with the four-coordinate palladium atom Pd(1) on the inversion center with a square planar geometry. The deprotonated L ligands are coordinated to the palladium ion in a chelate bidentate mode through the carbonyl oxygen O(1) and the azomethine nitrogen N(1) (O(1)—Pd(1)—N(1) = 92.05(14)°). The Pd(1)—O(1) bond distance (Pd(1)—O(1) = 1.968(3) Å) is slightly shorter than the Pd(1)—N(1) bond distance (Pd(1)—N(1) = 1.996(4) Å). In contrast, in complex [bis-(N-ethylsalicylaldimine)palladium] found in the literature, the Pd—O1 distance (1.94 Å) is much longer than the Pd—N1 distance (1.86 Å) [51].

A thorough search of the Cambridge Crystallographic Data Centre concerning the reported crystal structures of metal complexes with 2-(ethyliminomethyl)-phenol and its derivatives as ligands has revealed the following:

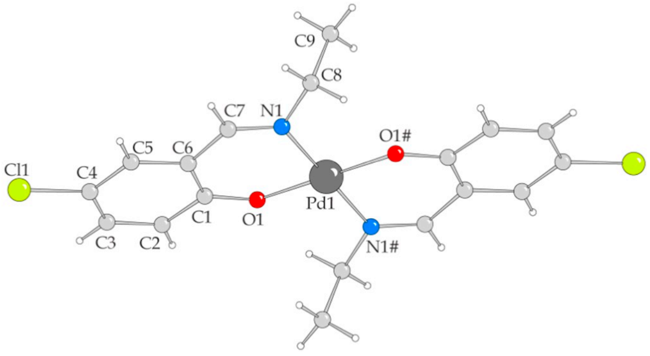

Fig. 1. Molecular structure of complex **1** with the displacement ellipsoids shown at the 50% probability level.

(a) regarding the nature of the metal, crystal structures of a variety of transition metal ions including Ti(IV) [52], Mn(IV) [53,54], Co(II) [55,56], Co(III) [57], Ni(II) [58–62], Cu(II) [63-69], Zn(II) [62,70], Zr(IV) [71,72], Ru(III) [73], Pd(II) [51], Au(III) [74,75] as well as Th (IV) [76] have been reported.

(b) regarding the substitution of the aromic ring, metal complexes with alkyl (tBu- [72], methyl- [62,73]), alkoxy (methoxy- [54]) and (di) halogen (chloro- [58,68], dichloro- [57,61], bromo- [61] and dibromo- [55]) groups have been also structurally characterized.

(c) regarding the presence of halogen group(s) as substitute(s) in the aromatic ring of 2-(ethyliminomethyl)-phenolate ligands, the crystal structures of Co(II) (for 3,5-dibromo-) [55], Co(III) (for 3,5-dichloro-) [57], Ni(II) (for 5-chloro-, 5-bromo- and 3,5-dichloro-) [58,60,61], and Cu(II) (for 5-chloro-) complexes exist; *i.e.* there are two more complexes, a mononuclear Ni(II) [58] and a dinuclear Cu (II) [68] one, bearing 5-chloro-2-(ethyliminomethyl)-phenolate ligands as complex **1**.

(d) the structure of one more palladium complex with 2-(ethyliminomethyl)-phenolate ligands [51] has been reported.

(e) three discrete coordination modes of these ligands have been observed (I–III as shown in Fig. 2); *i.e.* the monodentate mode where the coordination to the metal takes place *via* the phenolate oxygen atom (mode I), the bidentate fashion when the ligand is bound to metal *via* the phenolate oxygen and the imine nitrogen leading to the formation of a six-membered chelate (mode II) and the tridentate mode upon coordination of the ligand *via* the imine N to one metal and *via* the phenolate O to two metal ions forming a monoatomic O bridge (mode III). Mode III has been observed in the case of dinuclear Cu(II) complexes [63,66-69], while mode II is the often and has been observed in all other cases [51–65,70-76], and also in complex **1**. Mode I has been observed only in the crystal structure of a Ti(IV) complex [52] and only in co-existence with mode II.

3.3. Spectroscopic characterization of the complex

Infrared spectroscopy has confirmed the deprotonation and the coordination of HL. In the IR spectra of complex **1**, no peaks attributed to the stretching and bending vibrations of the phenolic OH around 3200 cm^{-1} and 1400 cm^{-1}, respectively, were observed and my suggest the deprotonation of the phenolic group of HL. In addition, the band originating from the C–O stretching vibration at 1285 cm^{-1}, exhibits in the IR spectra of the complex a shift to 1308 cm^{-1} implying coordination through the phenolate oxygen of the ligand [77,78]. The band assigned to the ν(C=N) of the ligand is located at 1662 cm^{-1}, and may denote the coordination of the ligand to the metal through the nitrogen.

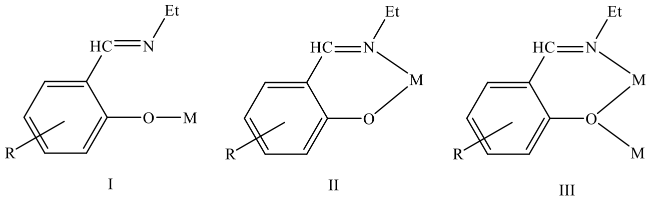

Fig. 2. Coordination modes of 2-(ethyliminomethyl)-phenol and its derivatives (R = tBu-, Me-, MeO-, Cl-, Br-, Cl,Cl-, Br,Br-) as ligands. (I) Monodentate, (II) bidentate, (III) tridentate.

^{1}H NMR spectroscopy was also used in order to confirm the formation and the deprotonation of the Schiff base ligand (L), as well as the stability of the complex in solution. The deprotonation of the phenolic hydrogen may be concluded by the absence of any –OH signal, which was observed in the ^{1}H NMR spectra of the free 5-Cl-saloH as single peak at $\delta = 12$ ppm. The signals expected for the aromatic protons of L were found in the range 8.06–6.77 ppm, whereas the signal attributable to the ethyl protons of L were observed at 3.83 ppm and 1.25 ppm for the $-CH_2$ and the $-CH_3$ groups, respectively (Fig. S2). The absence of any additional signals which might be related to dissociated ligands may indicate that complex **1** remains intact in solution keeping its structure.

In the UV–vis spectra of complex **1**, two bands attributable to d-d transitions were observed; the first one as a shoulder at 445 nm and the second one as distinct broad band at 397 nm. According to literature, for four-coordinate palladium(II) complexes with a square planar geometry around palladium, three d-d transition bands are expected in the regions 460–520 nm, 405–420 nm and 320–380 nm [79,80] which may be attributed to transitions from ground state ($^1A_{1g}$) to the excited states $^1A_{2g}$, $^1B_{1g}$ and $^1E_{1g}$, respectively. In the case of complex **1**, these bands are rather close and seem to overlap; the band at 445 nm may be assigned to the first transition while the remaining two transitions are ascribed to the second high-intensity band at 397 nm.

The UV–vis spectra of the complex were also recorded as nujol mull and in buffer solutions used for the biological experiments and present similar pattern with those recorded in DMSO solution. The combination of data derived from molar conductivity measurements, ESI-MS, ^{1}H NMR and UV–vis spectroscopy may leads us to conclude that the complex retains its structure in solution within the timeframe used for the biological experiments.

3.4. Interaction of complex 1 with CT DNA

The interaction of metal complexes with CT DNA usually takes place in a covalent and/or non-covalent fashion. In covalent interactions, one or more labile ligand(s) of the complex may be displaced by a nitrogen atom of a DNA-base (*i.e.* guanine-N7) leading to the formation of novel covalent bond(s) between the metal and DNA-nitrogen atom(s). The non-covalent interactions usually occur in the case of stable metal complexes and include three main modes, *i.e.* (i) intercalation through the insertion of the complex in-between DNA-base pairs resulting in the appearance of π-π stacking interactions, (ii) groove-binding to the major and/or minor groove mainly through van der Waals interactions and hydrogen bonding and (iii) electrostatic interaction to the external phosphate groups of the DNA-helix *via* Coulomb forces [81,82].

UV–vis spectroscopic titrations were employed as a preliminary approach to explore the existence of any interaction between the compound and CT DNA and to calculate the binding strength of this interaction. Any noncovalent interaction with DNA may perturb the band of CT DNA or the intra-ligand band(s) of the complex during these titrations [82].

So the UV–vis spectra of a DNA solution were recorded in the presence of increasing concentration of complex **1** (Fig. 3(A)). Addition of **1** into DNA solution resulted in slight hyperchromism of the DNA band at 258 nm, which may be attributed to the formation of a new adduct of **1** with double-helical DNA [83]. Additionally, a slight hyperchromism of the intraligand band at 397 nm was observed in the UV–vis spectra of

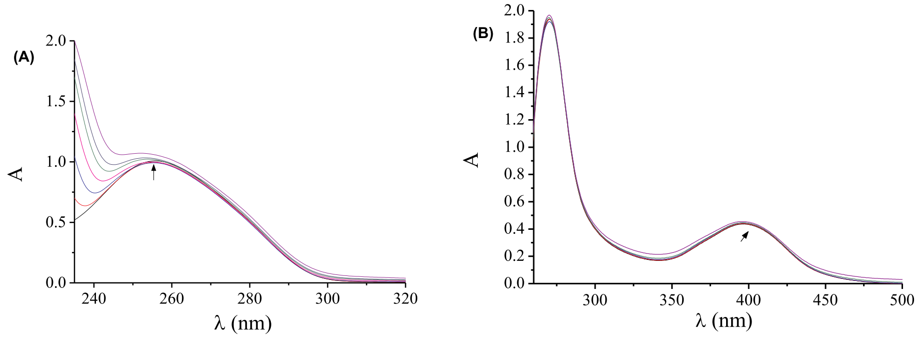

Fig. 3. UV–vis spectra of a solution of: (A) CT DNA ([DNA] = 1.5 × 10^{-4} M) in buffer solution (150 mM NaCl and 15 mM trisodium citrate at pH 7.0) in the presence of increasing amounts of complex **1** (*r* = [complex]/[DNA] = 0–0.5). The arrow shows the changes upon increasing amounts of complex **1**. (B) complex $[Pd(L)_2]$ (10^{-4} M) in DMSO in the presence of increasing amounts of CT DNA (*r′* = [DNA]/[complex] = 0–0.5). The arrow shows the changes upon increasing amounts of CT DNA.

complex **1** (Fig. 3(B)) upon the addition of increasing amounts of CT DNA. The changes observed in the UV spectra are not really intense and the existing spectroscopic features may not reveal a definite conclusion regarding the DNA-binding mode of **1** [82]; therefore, further DNA-viscosity measurements were conducted in order to shed light to the DNA-binding mode.

The K_b constant of complex **1** was obtained by the plot [DNA] / ($\varepsilon_A - \varepsilon_f$) *versus* [DNA] (Fig. S3) and the Wolfe-Shimer equation (Eq. (S1)) [84]. The K_b constant of complex **1** was found equal to 4.30 (± 0.74) × 10^4 M^{-1} (Table 1) and has the same magnitude with a series of reported Pd complexes with derivatives of carboxamides or salicylaldehydes as ligands found in the literature [42,85,86].

The relative DNA-viscosity (η/η_0) is sensitive to changes of the relative DNA-length (L/L_0) upon the interaction of DNA with a compound, because of the equation $(L/L_0) = (\eta/\eta_0)^{1/3}$ [87]. As known, an intercalative interaction will result in an increase of the separation distance of base pairs lying at intercalation sites in order to host the inserting compound, inducing an increase of the length of the DNA-helix and, subsequently an increase of DNA viscosity will be observed, the magnitude of which is usually in accordance to the strength of the interaction. In the case of a partial or non-classic intercalation (*i.e.* electrostatic interaction or external groove-binding), a bend or kink in the DNA-helix may occur, leading to a slight shortening of its effective length, and the relative DNA-viscosity may present a less pronounced decrease or even remain unchanged [87]. These characteristics may be proved helpful in clarifying the interaction with DNA.

The viscosity measurements were carried out on CT DNA solutions (0.1 mM) at room temperature upon addition of increasing amounts (up to the value of r = 0.35) of **1** (Fig. 4). Therefore, the increase of relative DNA-viscosity shown in the presence of complex **1** may be considered evidence of an intercalative interaction of complex **1** in-between the DNA-bases.

A solution containing the EB-DNA conjugate shows an intense fluorescence emission band at 592 nm (with $\lambda_{excitation}$ = 540 nm) as a result of the intercalation of the planar EB-phenanthridine ring in-between adjacent DNA-base pairs; for this reason, EB is considered a typical indicator to study the intercalation of a compound to DNA. If an intercalating compound which can bind to DNA equally or stronger than EB is added into this solution, a significant quenching of the EB-DNA fluorescence emission may be induced. The solution of complex **1** does not show any fluorescence emission bands at room temperature either alone or in the presence of DNA or EB under the same experimental conditions ($\lambda_{excitation}$ = 540 nm). Therefore, the changes in the fluorescence emission spectra of the EB-DNA solution, when complex **1** is added, may be informative regarding the EB-displacing ability of the complex [88].

Table 1
Binding, Stern-Volmer (K_{SV}) and quenching constants (k_q) regarding the interaction of complex 1 with DNA, HSA and BSA and its competition with EB.

Constant	1
$K_{b(DNA)}$ (M^{-1})	4.30 (± 0.74) × 10^4
$K_{SV(EB)}$ (M^{-1})	5.87 (± 0.27) × 10^4
$k_{q(EB)}$ (M^{-1} s^{-1})	2.55 (± 0.12) × 10^{12}
$K_{SV(BSA)}$ (M^{-1})	9.06 (± 0.40) × 10^4
$k_{q(BSA)}$ (M^{-1} s^{-1})	9.06 (± 0.40) × 10^{12}
$K_{(BSA)}$ (M^{-1})	2.43 (± 0.11) × 10^4
$K_{SV(HSA)}$ (M^{-1})	3.91 (± 0.17) × 10^4
$k_{q(HSA)}$ (M^{-1} s^{-1})	3.91 (± 0.17) × 10^{12}
$K_{(HSA)}$ (M^{-1})	3.21 (± 0.14) × 10^4

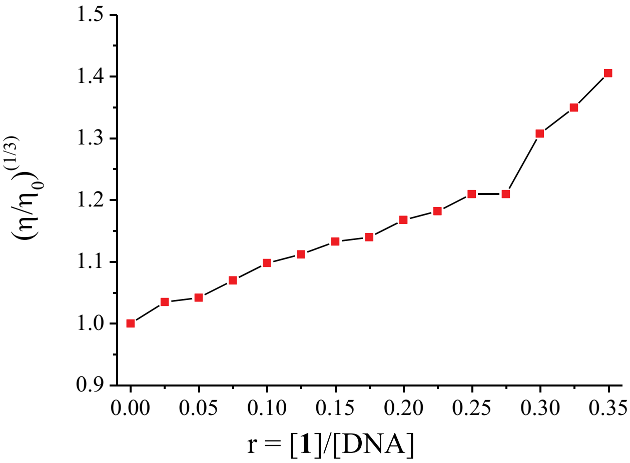

Fig. 4. Relative viscosity $(\eta/\eta_0)^{1/3}$ of CT DNA (0.1 mM) in buffer solution (150 mM NaCl and 15 mM trisodium citrate at pH 7.0) in the presence of complex **1** at increasing amounts (r = 0–0.36).

The fluorescence emission spectra of pre-treated EB-DNA ([EB] = 20 μM, [DNA] = 30 μM) were recorded (Fig. 5) in the presence of increasing concentration of complex **1** (up to r = 0.46). The addition of the complex resulted in a moderate-to-significant quenching (up to 62.3% of the initial EB-DNA fluorescence emission intensity) of the fluorescence emission band of the initial DNA-EB compound at 592 nm, showing the potency of **1** to displace EB for the EB-DNA conjugate. According to the Stern-Volmer plots (Fig. S4), the EB-DNA fluorescence emission quenching is in good agreement (R = 0.99) with the linear Stern-Volmer equation (Eq. (S2)); thus, the observed quenching may be attributed to the displacement of EB from EB-DNA by each complex and let us conclude indirectly an intercalative mode of interaction between complex **1** and CT DNA [89].

The calculated K_{SV} constant of **1** is equal to 5.87 (± 0.27) × 10^4 M^{-1} and is relatively high suggesting tight binding to DNA. The fluorescence lifetime of EB-DNA system is τ_o = 23 ns [90], the EB-DNA quenching constant of complex **1** (calculated with Eq. (S3)) is 2.55 (± 0.12) × 10^{12} M^{-1} s^{-1}. The k_q constant of **1** is significantly higher than 10^{10} M^{-1} s^{-1} [89] and may suggest that the quenching of the EB-DNA fluorescence takes place *via* a static quenching mechanism [91].

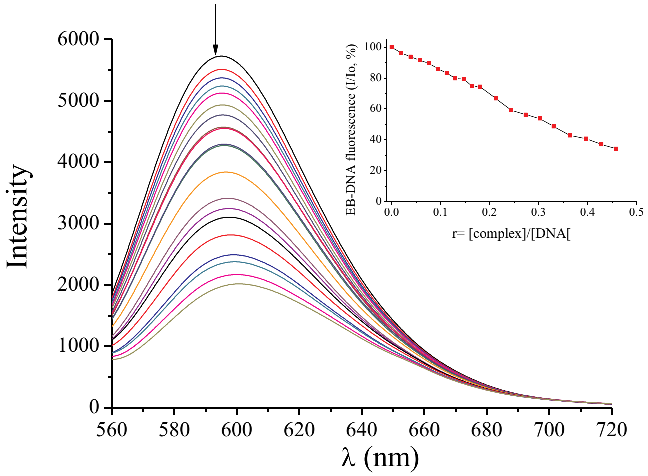

Fig. 5. Fluorescence emission spectra ($\lambda_{excitation}$ = 540 nm) for EB-DNA ([EB] = 20 μM, [DNA] = 26 μM) in buffer solution in the absence and presence of increasing amounts of complex **1** (up to r = 0.05). The arrow shows the changes of intensity upon increasing amounts of **1**. Inset: Plot of EB relative fluorescence emission intensity at $\lambda_{emission}$ = 592 nm (I/Io, %) *versus r* (*r* = [complex]/[DNA]) (up to 62.3% of the initial EB-DNA fluorescence intensity for **1**).

3.5. Interaction of complex 1 with plasmid DNA

The DNA interaction efficiency of a compound may be estimated after DNA treatment with it by its effect on the pDNA bands mobility and integrity, as visualized in agarose gel electrophoresis. A delayed mobility of pDNA (up shift) could be attributed to the binding of the compound to pDNA, increasing consequently, its molecular weight. Concerning DNA topology, the supercoiled conformation of pDNA (S) or covalently closed circular pDNA (ccc), due to its high folding and coiling degree, migrates faster than the relaxed conformation (R) or open circular (oc). At the side of the pDNA integrity, diminution or disappearance of the pDNA forms' amount suggests pDNA degradation due to a strong interaction with the compound. At the side of the pDNA integrity, diminution or disappearance of the pDNA forms' amount suggests pDNA-degradation due to a strong interaction with the compound.

The effect of the pDNA treatment with complex **1** is depicted for 30 min (Fig. 6(A1)) and 1 h (Fig. 6(A1′)) at concentrations 5–500 μM and 0.5–5 mM (Fig. 6(A2)). In both cases, a small delayed electrophoretic mobility (an up-shift) of both pDNA forms (supercoiled and relaxed) was observed, evidently, due to the pDNA binding with complex **1**. It is strange that, at the concentration of 60 μM, an obvious decrease of the relaxed (R) form occurred and a band is created which proceeds from the supercoiled pDNA and migrate ahead of all the other forms of the plasmid in a gel suggesting the formation of single-stranded closed-circles or a more compact form of supercoiled pDNA, which exhibit faster electrophoretic mobility due to the interaction with compound **1** (Fig. 6(A1 and A1′), lane 5). Furthermore, when higher concentrations of the complex were tested a delay of the electrophoretic mobility (up shift) of both pDNA forms occurs (Fig. 6(A2)) confirming the binding, while at concentration of 5 mM, the relaxed form is completely degraded as deduced by its complete disappearance (Fig. 6(A2), lane 6).

A similar strong up-shift of the pDNA bands was also observed with platinum complexes [92,93] as well as with other metal complexes [94,95] and nanoparticles [96].

3.6. Interaction of complex 1 with serum albumins

Serum albumins are the major soluble protein constituents of the circulatory system. Among their many physiological functions [97], the most important one is to transport drugs and other bioactive small molecules and ions through the bloodstream [97,98]. BSA has been the most extensively albumin studied in the literature, mainly because of its structural homology with HSA [99]. BSA consists of three homologous domains (I, II, III) and has two tryptophans, Trp-134 and Trp-212, located in the first sub-domain IB and sub-domain IIA, respectively. HSA is a globular protein composed of 585 amino acid residues in three homologous a-helices domains (I-III) bearing only one tryptophan found at position 214 along the chain and in sub-domain IIA [99,100]. The solutions of BSA and HSA exhibit an intense fluorescence emission band, due to the tryptophan residues, at $\lambda_{em,max}$ = 342 nm and 351 nm, respectively, when they are excited at 295 nm [101]. The solution of complex **1** did not exhibit any appreciable emission band, under the same experimental conditions. Furthermore, the inner-filter effect was evaluated with Eq. (S4); it was found too negligible to affect the measurements [102].

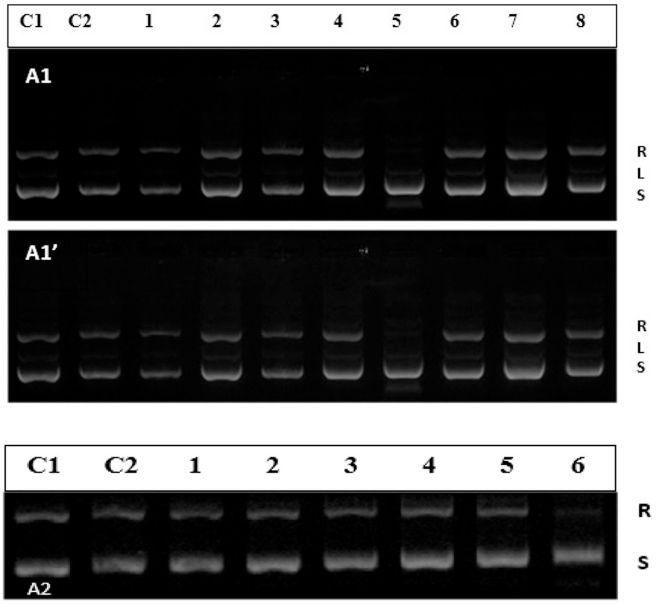

Fig. 6. Agarose (1% w/v) gel electrophoretic pattern of EB-stained mixture of supercoiled (S) and relaxed (R) plasmid DNA [**pBluescript SK**(+)], after 30 min and 1 h duration of electrophoresis. Each sample containing 5 μL (8 μg) of pDNA-incubated with **1** at 37 °C (A1): Lanes C_1, C_2: Controls, pDNA with buffer A, pDNA with buffer A and DMSO, respectively. Lanes 1–8: pDNA treated for 30 min (A1) and 1 h (A1′) with 5 μM, 10 μM, 20 μM, 40 μM, 60 μM, 100 μM, 200 μM, 500 μM of **1**, respectively. (A2) Lanes C_1, C_2: Controls, pDNA with buffer A, pDNA with buffer A and DMSO, respectively. Lanes 1–6: pDNA treated with 0.5 mM, 1 mM, 2 mM, 3 mM, 4 mM, 5 mM of **1**, respectively, for 1 h.

The addition complex **1** to a SA solution induced a low-to-moderate quenching of the respective SA fluorescence emission band (*i.e.* at λ_{em} = 351 nm for HSA and at λ_{em} = 342 nm for BSA) which is in the case of BSA was more pronounced (Fig. 7). This SA-quenching may be attributed to changes occurring in tryptophan environment of SA resulting from possible changes in secondary SA-structure due to binding of compound **1** [103]. The k_q constants for compound **1** (Table 1) were calculated from the Stern-Volmer plots (Figs. S5 and S6) and the Stern-Volmer quenching equation (Eqs. (S2) and (S3)); the values were found 9.06 ($\pm$ 0.40) $\times 10^{12}$ M^{-1} for BSA and 3.91 ($\pm$ 0.17) $\times 10^{12}$ M^{-1} for HSA. The k_q constants of the complexes are higher than the value 10^{10} M^{-1} s^{-1} suggesting the existence of static quenching mechanism that may indirectly confirm the interaction of complex **1** with the albumins [89].

The SA-binding constants (K) of the compounds for both SAs were calculated from the corresponding Scatchard plots (Figs. S7 and S8) and the Scatchard equation (Eq. (S5)); the K values of **1** were equal to 2.43

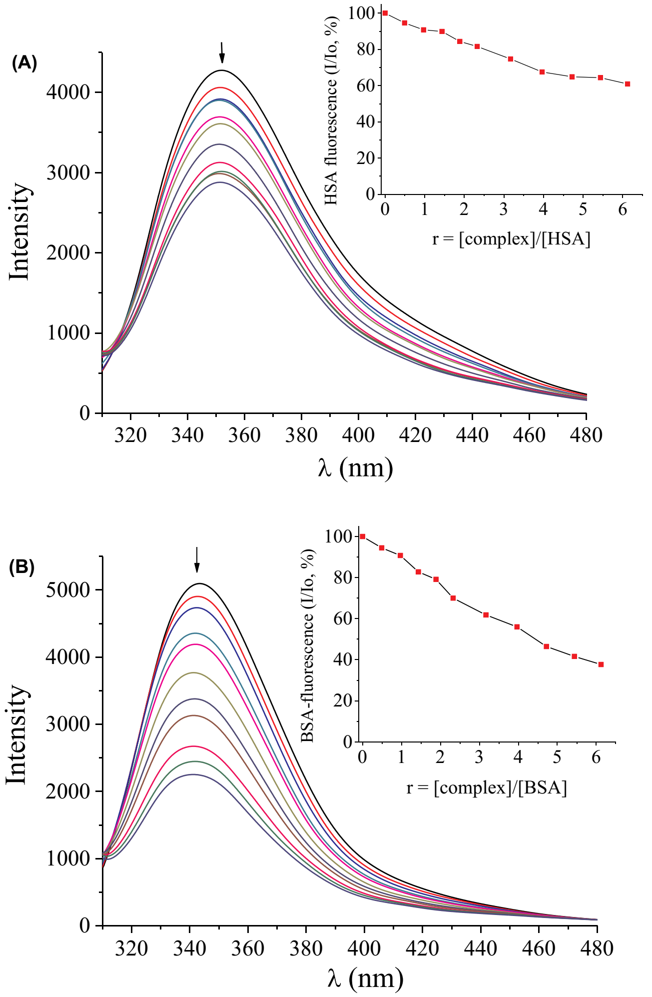

Fig. 7. (A) Fluorescence emission spectra ($\lambda_{excitation}$ = 295 nm) for HSA ([HSA] = 3 μM) in buffer solution (150 mM NaCl and 15 mM trisodium citrate at pH 7.0) in the absence and presence of increasing amounts of complex **1**. The arrow shows the changes of intensity upon increasing amounts of **1**. Inset: Plot of relative fluorescence emission intensity of HSA at λ_{em} = 351 nm (I/Io, %) *versus r* (*r* = [complex]/[HSA]) for complex **1** (up to 60.9% of the initial HSA fluorescence). (B) Fluorescence emission spectra ($\lambda_{excitation}$ = 295 nm) for BSA ([BSA] = 3 μM) in buffer solution (150 mM NaCl and 15 mM trisodium citrate at pH 7.0) in the absence and presence of increasing amounts of complex **1**. The arrow shows the changes of intensity upon increasing amounts of **1**. Inset: Plot of relative fluorescence emission intensity of BSA at λ_{em} = 342 nm (I/Io, %) *versus r* (*r* = [complex]/[BSA]) for complex **1** (up to 37.7% of the initial BSA fluorescence).

(± 0.11) × 10^4 M^{-1} for BSA and 3.21 (± 0.14) × 10^4 M^{-1} for HSA. The SA-binding constants of complex **1** are of the same magnitude with those reported for diverse palladium complexes with carboxamides or semicarbazones as ligands reported in the literature [42,85,86]. Furthermore, the magnitude of K constants may indicate the tight binding of complex **1** to the SAs in order to get transported toward the possible biological targets. It should be also noted that, upon arrival at these biotargets, the compound may have the potential to get released, since its noncovalent interaction with the SAs is less tighter than the strongest known noncovalent (irreversible) binding attributed to the interaction of diverse ligands to the protein avidin with K value ≈ 10^{15} M^{-1} [104,105].

3.7. Evaluation of antibacterial activity of complex 1

Table 2
Antibacterial activity of complex **1** evaluated by the Half-Minimal Inhibitory Concentration (IC_{50}, in μg/mL) and Minimal Bactericidal Concentration (MBC, in μg/mL) values provided by a nonlinear curve fit-growth/sigmoidal-dose response on the experimental optical density data. Values are mean of two replicates.

Microbial strains	1	1
	IC_{50} (μg/mL)	MBC (μg/mL)
Gram negative		
E. coli	Not detected	Not detected
X. campestris	> 100	160
Gram positive		
S. aureus	Not detected	Not detected
B. cereus	> 100	130
B. subtilis	94	110

The results of the antibacterial efficacy of the Pd(II) complex **1** against the five bacterial species (*E. coli*, *X. campestris*, *S. aureus*, *B. subtilis* and *B. cereus*) are presented in Fig. S9 and the IC_{50} and Minimal Bactericidal Concentration (MBC) values are cited in Table 2.

The Pd(II) complex **1** paradoxically at low concentrations seems to favor bacterial growth of almost all the bacteria except *E. coli* that it is not at all infected, while shows bactericidal activity only for *B. subtilis* from concentration higher than 100 μg/mL (Fig. S9). Although Pd(II) complexes have shown noteworthy antibacterial activity, regarding other studies [92], in this study the newly synthesized complex of Pd(II) seems to be a significant source of nutrients for the bacteria at the low concentrations tested.

3.8. Molecular docking calculations

Molecular docking calculations were employed to evaluate the ability of complex **1** to bind to macromolecules HSA, BSA, CT DNA and DNA-gyrase, in order to explain the *in vitro* activity of this compound. Binding energies for the best docking poses of complex **1** with HSA, BSA, CT DNA and DNA-gyrase are shown in Table 3. The binding interactions of complex **1** with HSA, BSA, CT DNA, and DNA-gyrase are illustrated in Tables S2–S5. The molecular structural organization of HSA and BSA provides a variety of ligand binding sites shown in Fig. S10. The secondary structures of HSA and BSA shown with the subdomains color-coded are assigned based on Sugio et al. [106] and Bujacz et al. [107], respectively.

The computational approach revealed that complex **1** is anchored in a cavity of HSA protein in sub-domain IIIB formed by helices IIIB-h10, IIIB-h9 and IIIB-h8 (Ligand-Binding Domain (LBD) 1, LBD1), in binding site V (Fig. 8, upper part). Complex **1** can also be stabilized, less favorably, in another binding pocket between binding sites I, II and IV (LBD2) formed by helices IIIA-h3, IIIA-h4 and IIA-h1 (Fig. 8, lower part, the designation of sub-domains and helices are shown in Fig. S10). Hydrogen-bond (H-b), polar (P) and hydrophobic (H-ph) contacts of the

Table 3
Global binding energies (in kcal/mol) of complex **1** docked on HSA, BSA, CT DNA and DNA gyrase targets (Protein Data Bank (PDB) accession numbers: 2BXG, 4OR0, 1BNA and 1KZN, respectively) along with the occupied drug binding sites (BSs) in Ligand-Binding Domains (LBDs) 1 and 2 (* denotes common binding site with co-crystallized drug naproxen (NPS)).

Complex 1	HSA	BSA	CT DNA	DNA gyrase
Lowest energy (most favorable binding pose)	− 42.22 LBD1 - BSV	− 37.13 LBD1 - BSIII*	− 28.94	− 42.78
Higher energy (next favorable binding pose)	− 37.46 LBD2 - Between BS's I, II, IV	− 36.83 LBD2 - Between BS's I, II, IV	− 28.02	− 30.53

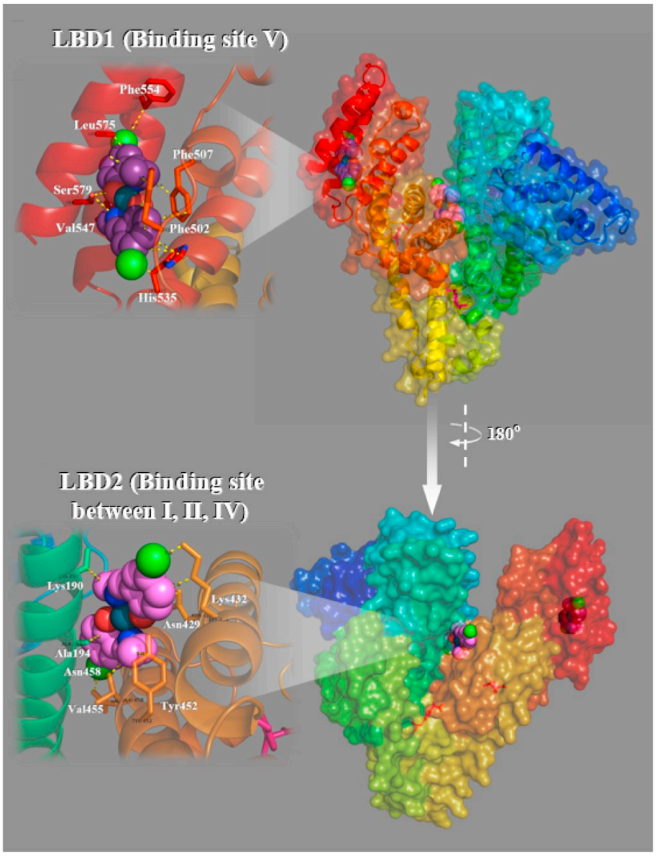

Fig. 8. Docking poses of complex **1** superimposed with the co-crystallized drug ibuprofen (IBP) into HSA (PDB ID 2BXG) (chain A). Target protein is illustrated as cartoon with sub-domains color-coded according to chainbow, with additional depiction of semi-transparent surface colored also by chainbow. Two individual poses for both complex **1** and IBP in the most common binding sites: site V and between sites I, II and IV for complex **1**, and site III and IV for IBP are depicted. Complex **1** is represented as CPK spheres colored according to atom type (deep purple or violet C atoms) and IBP molecules are depicted in stick model and colored according to atom type in hot pink C atoms. Complex **1** in its lower energy binding pose (LBD1) (deep purple C atoms) is anchored in binding site V, in the cavity formed by helices IIIB-h10, IIIB-h9 and IIIB-h8 (upper part), while docking simulation resulting in next higher energy pose placed it in LBD2 (violet C atoms), in a crevice formed by helices IIIA-h3, IIIA-h4 and IIA-h1, revealed by a rotated view of the initial structure by 180 degrees around the main vertical axis of heart-shaped protein (the designation of sub-domains and helices are shown in Fig. S9). Selected side chain residues in the binding network are shown as sticks color-coded by chain. Heteroatom color-code: Cl: green, N: blue, O: red, Pd: petrol. Binding contacts are shown as yellow dotted lines. Molecular docking simulations of both ligands were performed individually. H atoms are omitted for clarity. The final structure was ray-traced and illustrated with the aid of PyMol Molecular Graphics System. Binding interactions are shown in Table S2.

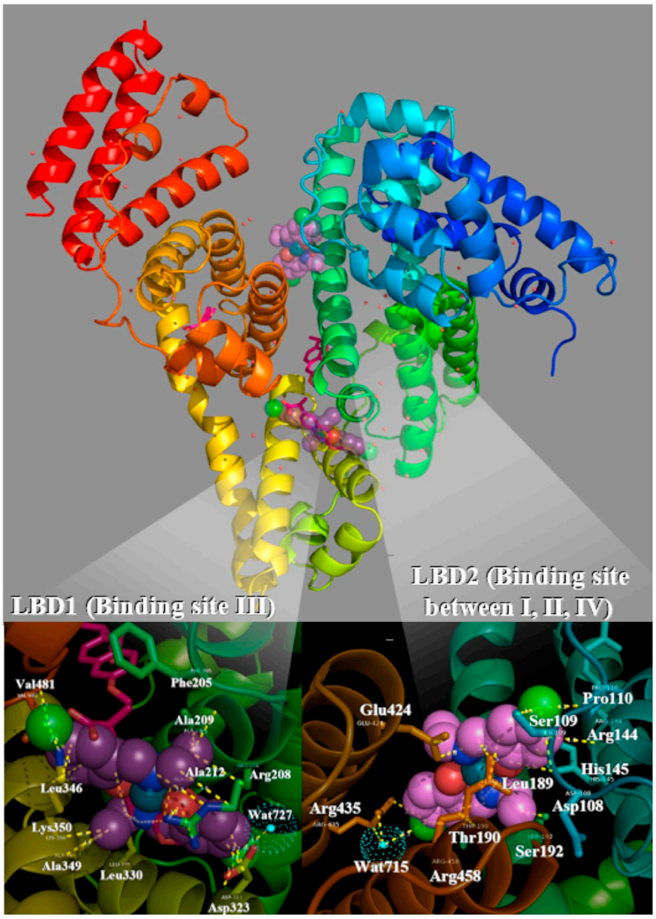

Fig. 9. Docking poses of complex **1** superimposed with the co-crystallized drug NPS into BSA (PDB entry code 4OR0) (chain A). The best poses for complex **1** and NPS (in two binding pockets) in the most common binding sites: site III designated as LBD1 between sub-domains IIA, IIB and IIIA, and between sites I, II and IV (the designation of sub-domains and helices are shown in Fig. S9) designated as LBD2 between sub-domains IB, IIA and IIIA. Complex **1** is docked in the LBD1 cavity surrounded by helices IIA-h2 and IIB-h9 (most favorable binding with lower binding energy), and LBD2 cavity surrounded by helices IIA-h1, IIIA-h4 (second most favorable binding with higher binding energy), while for NPS there are depicted three individual poses in the binding sites III and IV. Complex **1** is illustrated in sphere representation, while NPS is depicted in stick model. Both molecules are colored according to atom type: deep purple C atoms for complex **1** in LBD1 and violet C atoms in LBD2, and hot pink C atoms for NPS. Target protein is illustrated as cartoon with sub-domains color-coded according to chainbow, with additional depiction of semitransparent surface colored also by chainbow. A close up view of the binding cavities of complex **1** labeled as LBD1 and LBD2 is shown in lower part. Selected contacting amino acid residues of the binding pocket are rendered in stick model and colored according to atom type (LBD1) or chainbow (LBD2). Heteroatom color-code: Cl: green, N: blue, O: red, Pd: petrol. Binding contacts are shown as yellow dotted lines. Molecular docking simulations of both ligands were performed individually. H atoms are omitted for clarity. The final structure was ray-traced and illustrated with the aid of PyMol Molecular Graphics System. Binding interactions are shown in Table S3.

studied complex with the target protein HSA are illustrated in Table S2. It is obvious (Table S2) that complex **1** is predicted to bind to LBD1 of the protein with lower binding energy, compared to LBD2, reasoning a better stabilization in the protein's binding pocket, a fact that is in accordance with the more extended hydrogen bond network. Two H-bond contacts between phenyl oxygen and imino nitrogen atoms of Schiff base L of complex **1** and Ser579 residue, additionally contribute to the stabilization of the molecule in protein's binding pocket. Further stabilization of the docked molecule inside most energetically favorable LBD1 cavity is achieved with the participation of π-π interactions observed between aromatic ring of L and Phe507 and His535 residues and the construction of a hydrophobic cavity, formed by residues Leu575, Val547, Phe502, Val576, Phe507, and His535. Binding site LBD1 of complex **1** is adjacent to two sites in sub-domain IIIB, where the thyroid hormone thyroxine also binds [108].

The identified drug-binding sites of complex **1** in BSA protein, LBD1 and LBD2, are illustrated in Fig. 9. Docked molecule is positioned in drug-binding site III (most favorable LBD1) at the same place with the co-crystallized drug naproxen (NPS), in a cavity surrounded by helices IIA-h2 and IIB-h9. The second most favorable binding site revealed to be LBD2, formed by helices IIA-h1 and IIIA-h4 (the designation of sub-domains and helices are shown in Fig. S10). The binding interactions of

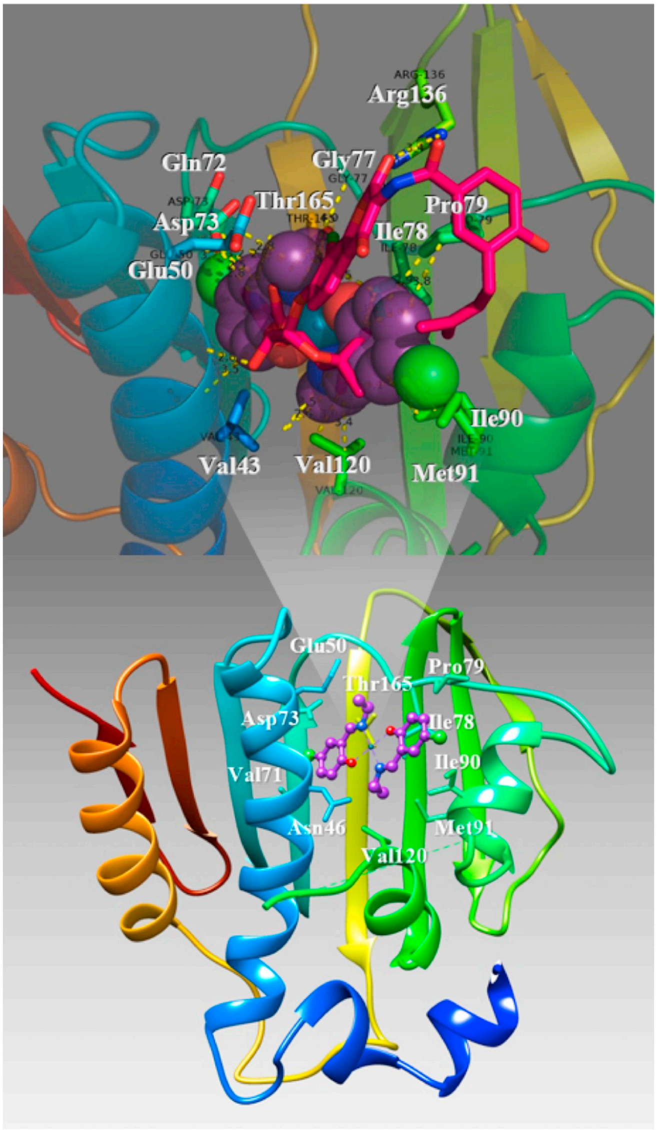

Fig. 10. Docking pose orientation of complex **1** (deep purple C atoms rendered in sphere mode) superimposed with CBN (hot pink C atoms rendered in stick representation) on DNA-gyrase (PDB ID: 1kzn). The ligand-binding site of the molecules depicting the extent of the pocket as determined by the computation process labeling the critical amino acid residues interacting with both molecules is shown in the upper part. Heteroatom color-code: Cl: green, N: blue, O: red, Pd: petrol. Binding contacts are shown as yellow dotted lines. Molecular docking simulations of both ligands were performed individually. H atoms are omitted for clarity. The final structure was ray-traced and illustrated with the aid of PyMol Molecular Graphics System (upper part) and UCSF Chimera visualization system (lower part). Binding interactions are shown in Table S4.

the docked molecule inside LBD1 and LBD2, involving hydrogen bond, hydrophobic and polar contacts, are shown in Table S3. An extended network of hydrophobic and hydrogen bond contacts in LBD1 explains the favorable accommodation of complex **1** inside this pocket. π-π interactions observed between aromatic ring of Schiff base HL and His145 residue additionally contribute to the stability of the molecular structure between complex **1** and BSA protein. As obvious from Table S3, complex **1** and NPS share a number of amino acid residues taking part in the anchorage of the molecules in LBD1 binding pocket.

We chose to use for docking experiments the DNA-gyrase in complex with bound co-crystallized drug chlorobiocin (CBN), which include only the B subunit exhibiting the crucial ATPase activity (A subunit is mainly involved in DNA-breakage and reunion) [109,110]. The binding of complex **1** in the crystal structure of DNA-gyrase, superimposed with the co-crystallized inhibitor CBN ligand, is depicted in Fig. 10, where the best-fitted docking pose of complex **1** inside the ATP-binding site of DNA-gyrase is shown. The compound is stabilized inside the same binding pocket of the protein, occupied by CBN [107]. CBN is one of the most important members of the coumarin family inhibitors of DNA-gyrase activity, by competitively binding to the ATP-binding site. The binding pocket is defined by a cavity of approximately 20 Å inside the B subunit of the protein which consists of two domains, an N-terminal domain of ~44 kDa and a C-terminal one of 47 kDa. The N-terminal domain includes two sub-domains (24 kDa C-terminal part and 20 kDa N-terminal part). The ATP-binding site is located in the first sub-domain of the protein, *i.e.* in the C-terminal part of the N-terminal domain. Complex **1** is shown to lie at the entry of the catalytic pocket, partially covering the ATP-binding site. Stabilization of compound **1** may be attributed to hydrogen-bond, polar and hydrophobic contacts inside the ATP-binding site of DNA-gyrase protein. The docking predicts the formation of hydrogen bonds between the imino N atom of the Schiff base ligand and H-bond donors: OH of Thr165 and HND2 of Asn46 (Table S4). Aromatic C atoms of ligand L form additional hydrophobic contacts with Ile90, Ile78, Pro79 and Asp73 residues. A hydrophobic cavity is additionally constructed with the inclusion of residues Val120, Met91, Gly77 and Thr165. Complex **1** is further stabilized inside the protein's binding pocket with polar contacts with Asn46, Asp73, Val43, Thr165, and Gln72 residues. Common binding residues with CBN revealed to be Asn46 (also taking part in hydrogen bond), Ile90, Pro79, Asp73, Gly77, and Gln72, while the rest residues are sited in adjacent to those of CBN ligand [111,112].

Our model for predicted binding poses of complex **1** into CT DNA, suggests intercalation of the complex with A and B helices of DNA, between purines and pyrimidines of the same strand and between strands as well, in minor groove of DNA, due to the development of van der Waals forces, hydrogen or hydrophobic bonds (Table S5 and Fig. 11). Interaction of Cl atom with N9 guanine atom of DG22 in B-strand interrupts interstrand H-bond with its pair cytosine. The same is obvious for contacts of Cl atom with N2 guanine atom of DG4 in A-strand (interrupts H-bond with carbonyl O of its paired cytosine) and O2 cytosine atom of DC21 in B-strand (interrupts H-bond with NH2 of its paired guanine). The docking orientation of complex **1** in the crystal structure of CT DNA in the binding cavities of minor groove of DNA is shown in Fig. 11. Compound **1** seems to achieve its stabilization inside minor groove of DNA due to a hydrogen bonds formed between phenyl O and imino N of the Schiff base ligand and OH group of water96 and water78 molecules, respectively. Ligand-binding site architecture of the docked molecule in CT DNA crystal structure is illustrated in Fig. 11(b). Additional stabilization of complex **1** inside the minor groove of DNA is achieved by the formation of π-π interactions between phenyl ring carbon atoms of the Schiff base ligand with the aromatic rings of nucleotides DA6 and DG22 (Fig. 11 and Table S5). A construction of hydrophobic pocket is mediated with the inclusion of DA6, DT7 and DG22 nucleotides. Compound **1** is also interacting with the minor groove of DNA with five polar contacts with the participation of DG22, DC21 and DG4 nucleotides. Due to the bulk size of the complex, it enters the minor groove by its half size, *i.e.* one of its HL Schiff bases as is illustrated in Fig. 11(a).

3.9. Polypharmacology browser for target prediction in ChEMB

Furthermore, *in silico* predictive tools have been employed to identify new targets. The ability of complex **1** to interact with more than one target proteins was explored with Polypharmacology Browser. Target identification has become an area of intense research owing to widespread application ranging from the identification of the biological active molecule, drug re-purposing, toxicity prediction to the identification of promiscuous drugs or compounds (Poly-Pharmacology).

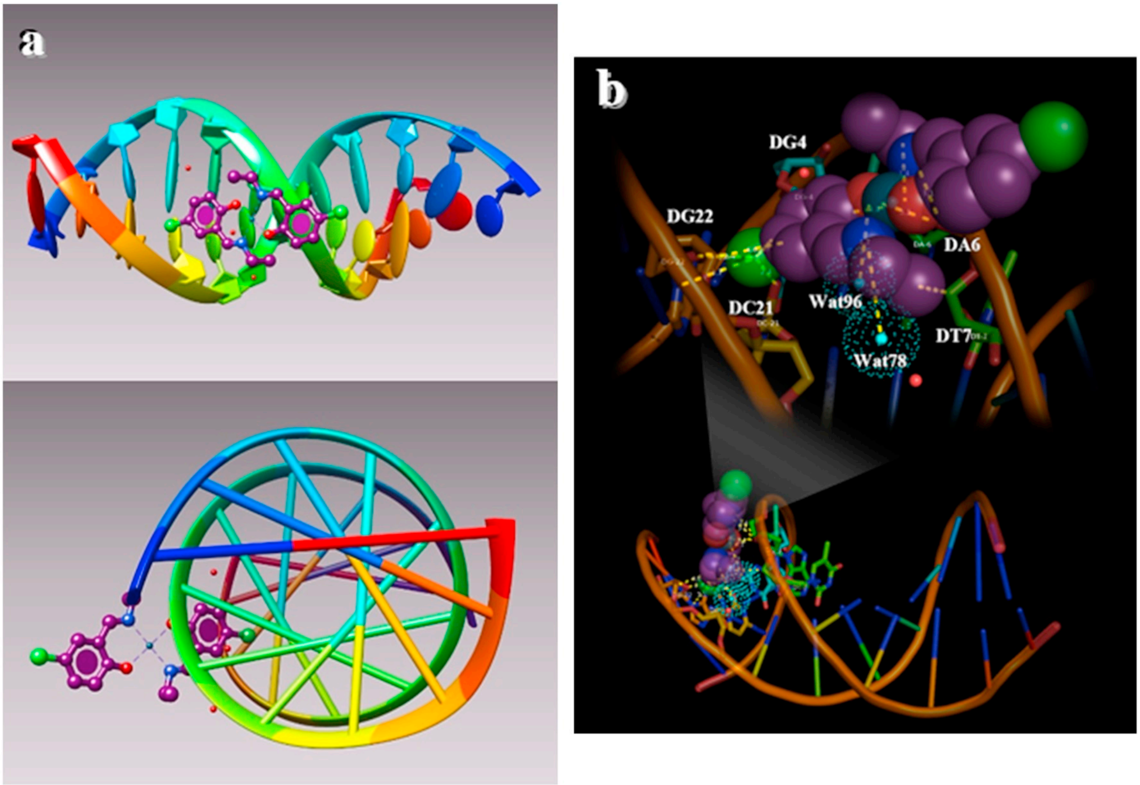

Fig. 11. Binding architecture of complex **1** in the crystal structure of CT DNA (PDB accession no. 1bna) depicting its stabilization in the binding cavity of minor groove of DNA. (a) DNA structure is illustrated with smooth ribbons colored in rainbow, stick bonds, and special representations of the sugars and bases created with the nucleotides extension of UCSF Chimera version 1.11, while complex **1** is rendered in ball-and-stick mode with deep purple C atoms. (b) In the ligand-binding site, DNA structure is illustrated as cartoon color-coded according to chain in brown color with the aid of PyMol Molecular Graphics System, while docked molecule is represented in sphere model and colored according to atom type (deep purple C atoms). The docking pose from a view above the axis of the helix to illustrate the extent of insertion of docked molecule in the interior of double strand DNA is illustrated In lower part of (a). Binding interactions with nucleotide molecules are shown in Table S4. Nucleotides are rendered in semitransparent stick model and colored according to atom type. Yellow dotted lines indicate hydrogen bond, polar and hydrophobic interactions between the docked molecule and the nucleotides of the binding pocket in the minor groove of DNA. H atoms are omitted from all molecules for clarity. Nucleotides are numbered according to PyMol software. The final structure was ray-traced.

Interactions of the drug molecule with unintended side targets (off-targets) often leads to adverse-drug reactions and shown to be one of the most common reason for the failure of drug molecule in the clinical trial. The Poly-pharmacology profile of complex **1** identifying probable target proteins is illustrated in Table S6. It is deduced (Table S6) that P = 0 for the following ChEMBL-Names and IDs of targets retrieved from a variety of fingerprints: 1) Thromboxane A2 receptor, TBXA2R (CHEMBL2069) in Topological Pharmacophore-Xfp, 2) fatty acid binding protein adipocyte, FABP4 (CHEMBL2083) in Topological Pharmacophore-Xfp, 3) fatty acid binding protein muscle, FABP3 (CHEMBL3344) in Topological Pharmacophore-Xfp, 4) prostaglandin E synthase 2, PTGES2 (CHEMBL4411) in Topological Pharmacophore-Xfp, 5) G protein coupled receptor 44, PTGDR2 (CHEMBL5071) in Topological Pharmacophore-Xfp, 6) aldose reductase, AKR1B1 (CHEMBL1900) in Topological Pharmacophore-Xfp, 7) sodium channel protein type IX alpha subunit, SCN9A (CHEMBL4296) in Atom-Pair fingerprint-APfp, 8) retinoid X receptor alpha, RXRA (CHEMBL2061) in Topological Pharmacophore-Xfp, 9) aryl hydrocarbon receptor, AHR (CHEMBL3201) in Extended-Connectivity Fingerprint-ECfp4, 10) Cyclooxygenase-1, PTGS1 (CHEMBL221) in Topological Pharmacophore-Xfp, 11) Cyclooxygenase-2, PTGS2 (CHEMBL230) in Topological Pharmacophore-Xfp, and 12) Cytochrome P450 2A5, CYP2A5 (CHEMBL4085) in Extended-Connectivity Fingerprint-ECfp4.

3.10. PASS biological activity prediction profile

Prediction of activity spectra is based on PASS technology which can predict over 4000 kinds of biological activity, including pharmacological effects, mechanisms of action, toxic and adverse effects, interaction with metabolic enzymes and transporters, influence on gene expression, *etc*.

3.10.1. Activity spectra prediction

The results of PASS prediction are given as a list of biological activities, for which the difference between probabilities to be active (Pa) and to be inactive (Pi) was calculated. The results for activity spectra prediction for complex **1** with Pa > 0.7 are reported in Table S7. The output file represents a list of predictable biological activities. It is interesting to note that the second place in the ranking is occupied for antineoplastic activity with Pa = 0.851, maybe because of its probable activity against a number of proteins involved in cancer growth.

3.10.2. CLC-Pred: in silico prediction of cytotoxicity for tumor and non-tumor cell lines

The *in silico* prediction of cytotoxic activity of complex **1** on a large number of cancer cell lines is shown in Table S8. It is deduced that for probability level higher than 0.7, only one cancer cell line, the brain derived oligodendroglioma Hs683, was found to be sensitive to complex **1**.

3.10.3. DIGEP-Pred: prediction of drug-induced changes of gene expression profile

The DIGEP-Pred of drug-induced changes of gene expression profile for complex **1** is shown in Tables S9–S14. With this *in silico* tool it is possible to estimate the influence of complex **1** on gene expression, based on mRNA, protein and activity related to human cancer cell lines MCF-7 (breast) and VCaP (prostate) and the combination prediction results, respectively. The output file represents a list of activities with two probabilities, Pa (probability to be active) and Pi (probability to be inactive). The more probable changes of gene expression are at the top of the list. Only the down-regulated and up-regulated target proteins predicted with a $Pa > 0.5$ are shown. From Table S9 it is interesting to notice that the two first entries with the highest Pa values (0.937) in the mRNA-based training set prediction of 500 up-regulation genes are *FABP4* (fatty acid binding protein 4) with $Pa = 0.748$ and *MYBL1* (MYB proto-oncogene like 1) with $Pa = 0.726$. The prediction of *FABP4* is in accordance with the previous PPB target prediction in ChEMB (Section 3.9), where FABP4 protein is positioned in the 2nd place of probable target proteins.

For mRNA based predictions and $Pa > 0.7$, two down-regulated genes were identified: *MYBL1* (MYB proto-oncogene like 1) and *FABP4* (fatty acid binding protein 4), while for upregulated genes, *REL* (*REL* proto-oncogene, NF-kB subunit) and *MGST1* (microsomal glutathione S-transferase 1), genes found to play a role. For protein based predictions (Table S10) and $Pa > 0.7$, it was identified one downregulated gene: *VIM* (vimentin). For up-regulated genes there was no result with $Pa > 0.7$. For MCF7 based predictions and $Pa > 0.7$, two genes were identified and only for the upregulation mode of action *DDX60* (DExD/H-box helicase 60) and *IFIT2* (interferon induced protein with tetratricopeptide repeats 2). For VCAP cells in 6 h, only one down-regulated gene was found in probability level of $Pa > 0.7$: HP (haptoglobin). Vimentin is found to be over-expressed in many tumor types [113]. Down-regulation of its protein could contribute to anticancer activity of complex **1**. Rel/NF-kappaB proto-oncogene transcription factors are key regulators of immune, inflammatory and acute phase responses and are also implicated in the control of cell proliferation and apoptosis [114]. This gene encodes a protein that belongs to the Rel homology domain/immunoglobulin-like fold, plexin, transcription factor (RHD/IPT) family. Members of this family regulate genes involved in apoptosis, inflammation, the immune response, and oncogenic processes. This proto-oncogene plays a role in the survival and proliferation of B lymphocytes. Mutation or amplification of this gene is associated with B-cell lymphomas, including Hodgkin's lymphoma. Persistent nuclear NF-kappaB activity was also described in several human cancer cell types, as a result of constitutive activation of upstream signaling kinases or mutations inactivating inhibitory IkappaB subunits. Experiments implicating NF-kappaB in the control of the apoptotic response also support a role in oncogenesis and in the resistance of tumor cells to chemotherapy.

For MCF-7 human breast cancer cells based predictions (Table S11), it was identified as downregulated the *DEK* gene which plays a role in steroid hormone receptor signaling in breast cancer, supporting cell proliferation, invasion and the maintenance of the breast cancer stem cell population [115]. *DxEK* oncogene expression is associated with positive hormone receptor status in primary breast cancers and is up-regulated *in vitro* following exposure to the hormones estrogen, progesterone, and androgen [116]. MCF-7 cells are known to be hormone positive (estrogen and progesterone receptor positive, ER+, PR+) and *DEK* is a target gene whose expression promotes estrogen-induced proliferation. Additionally, complex **1** from ADMET predicted profile-Classifications (Table S19) found to act as an ER and androgen receptor (AR) binder, due to estimated probability levels of 0.7039 and 0.6812, respectively. Since complex **1** is able to downregulate *DEK* gene in MCF-7 cells, this targeted inhibition of translated DEK protein may enhance the efficacy of conventional hormone therapies in breast cancer. Furthermore, the also downregulated gene *ALDH1A3*, encodes a metabolic target for cancer therapy and is associated with the development, progression, and prognosis of cancers [117]. ALDH1A3, as well as other members of the ALDH1 subfamily, can function in cells as a retinaldehyde dehydrogenase to generate retinoic acid (RA) from retinal. The enzymatic activity of ALDH1A3 and its product RA, are necessary for the observed expression of tissue transglutaminase (tTG) in mesenchymal (MES) glioma stem cells (GSCs). tTG, a dual-function enzyme with GTP-binding and acyltransferase activities, has been implicated in the survival and chemotherapy resistance of aggressive cancer cells and cancer stem cells (CSC), including glioma stem cells. Therefore, there is a link between tTG and ALDH1A3 since its upregulated expression in cancer stem cell populations. For this reason, it may be therapeutically targeted for various types of glioma cells. This result of downregulation of *DEK* gene by complex **1**, can also explain, in part, the results from cancer cell line prediction of cytotoxic activity of complex **1** (Table S8), revealing Hs 683 oligodendroglioma cell line to be sensitive to the activity of complex **1**.

3.10.4. SMP: prediction of substrate/metabolite specificity ($Pa > Pi$)

In Table S15 are illustrated the substrate and metabolite based specificity predictions for complex **1**. The interactions with metabolic enzymes and transporters are shown with their corresponding probability levels.

3.10.5. SOMP: prediction of sites of metabolism

For the prediction of SOMPs for complex **1**, sets for the five isoforms of CYP P450 that metabolize the majority of xenobiotics have been prepared: 3A4, 2C9, 2C19, 2D6 and 1A2. The reaction of glucuronidation was also included, which is catalyzed by UGT (Table S16). In Table S16 the SoLAs are illustrated, in which labeled atom is a SOM with positive ΔP values. The labeled atoms in SOM (ΔP+) revealed to be 11, 9, 11, 9, 9 and 2 atoms of complex **1** for CYP3A4, CYP2D6, CYP2C9, CYP2C19, CYP1A2 and UGT, respectively.

3.10.6. ROSC-Pred: rodent organ-specific carcinogenicity prediction ($Pa > Pi$)

No carcinogenicity was predicted for complex **1** and for probability level higher than 0.7 ($Pa > 0.7$), except for female mice and specifically for the thyroid gland organ, as is illustrated in Table S17.

3.11. ProTox-II - prediction of toxicity of chemicals

3.11.1. Oral toxicity prediction results

Predicted Lethal Dose value in mg/kg body weight (LD_{50}) and toxicity class for oral toxicity of complex **1** found to be 540 mg/kg (LD_{50}), and 4 (predicted toxicity class). The comparison of complex **1** with dataset compounds (training set of 38,515 compounds) is illustrated in Fig. S11, leading to the conclusion that complex **1** could be harmful if swallowed ($300 < LD_{50} \leq 2000$). Toxicity risk assessment parameters and drug related properties were within the acceptable interval which validate complex **1** as drug. The validation approach used is leave-one-out cross-validation with balanced accuracy of 0.86. The descriptors that were adopted were fragments and molecular fingerprints.

3.12. SwissTargetPrediction

In Table S18, are shown the target proteins with higher possibility for binding with complex **1**, derived from Swiss Target Prediction. Two of the proteins depicted in Table S18 with higher possibility to act as targets for complex **1**, are microtubule-associated protein tau (MAPT) and Cannabinoid receptor 1 (CNR1).

3.12.1. MAPT

Structural and biochemical alterations of the MAPT are associated with degenerative disorders referred to as tauopathies. We have previously shown that MAPT is present in human islets of Langerhans, human insulinomas, and pancreatic beta-cell line models, with biophysical similarities to the pathological MAPT in the brain. Furthermore, MAPT plays a role in pancreatic endocrine tissue. It was found upregulation of MAPT protein expression in human insulinomas when compared to human pancreatic islets of Langerhans and an imbalance between MAPT isoforms in insulinomas tissue [118]. MAPT may play an important role in insulin granule trafficking and indicate the importance of balanced MAPT phosphorylation and dephosphorylation for adequate insulin release. Aggregates of abnormally hyperphosphorylated MAPT are the main constituent of neurofibrillary tangles (NFTs) and neuropil threads (NTs) that are characteristic neuropathological hallmark lesions of Alzheimer's disease [119,120]. MAPT gene encodes the MAPT protein whose transcript undergoes complex, regulated alternative splicing, giving rise to several mRNA species. MAPT transcripts are differentially expressed in the nervous system, depending on stage of neuronal maturation and neuron type. MAPT gene mutations have been associated with several neurodegenerative disorders such as Alzheimer's disease, Pick's disease, frontotemporal dementia, cortico-basal degeneration and progressive supranuclear palsy.

3.12.2. CNR1

Cannabinoids have been shown to activate an Endoplasmic Reticulum ER-stress related pathway that leads to the stimulation of autophagy-mediated cancer cell death. In addition, cannabinoids inhibit tumor angiogenesis and decrease cancer cell migration [121]. CNR1 receptor was found to be upregulated in Hodgkin lymphoma cells [122] and in chemically induced cellular hepatocarcinoma [123]. CNR1 receptor levels are also increased and correlate with disease severity in human epithelial ovarian tumors [124] and have been proposed to be a factor of bad prognosis following surgery in stage IV colorectal cancer [125]. Cannabinoid treatment promotes cancer cell death, impair tumor angiogenesis and block invasion and metastasis [126]. The molecular mechanisms that have been proposed to be involved in cannabinoid anticancer actions have been thoroughly reviewed elsewhere [127,128].

3.13. ADME predictions

For the ADMET predictions, two methods were adopted, SwissADME and admetSAR.

3.13.1. SwissADME predictions

Physicochemical descriptors and predicted ADME parameters, pharmacokinetic properties, drug-likeness nature and medicinal chemistry friendliness and bioavailability radar, are depicted in Fig. S12. From the predicted descriptors it is deduced that complex **1** bears a good lipophilicity and human intestinal absorption (high). Furthermore, it is shown to be able to pass the blood brain barrier (BBB), to inhibit various CYP metabolism enzymes, to act as a P-glycoprotein substrate, and finally to possess drug likeness properties, since it is not violating none of the adopted rule tests (Lipinski, Ghose, Veber, Egan and Muegge).

3.13.2. admetSAR predictions

In Table S19 is illustrated a series of ADMET properties of complex **1**, leading to the conclusion that this compound, with high probability, could be absorbed by the intestinal (probability, 0.9898), enable Caco-2 cells permeability (probability, 0.8674), and pass the BBB (probability, 0.9807). Additionally, ER- and AR-binding of the compound could be a factor contributing to its possible anticancer activity. One undesired property of the compound is that it appears to be eye corrosive and irritant with probability levels 0.9772 and 0.9580, respectively. Carcinogenicity and Ames mutagenicity, could also play a limiting therapeutic role (probability levels 0.7857 and 0.7000, respectively), although organ-specific carcinogenicity was not predicted for probability level higher than 0.7. Nevertheless, Acute Oral Toxicity of 2.104 kg/mol, is a rather high value, maybe due to limited human oral bioavailability (probability level of 0.5429). Plasma protein binding (probability of 100%) is in a good agreement with *in vitro* and *in silico* molecular docking results.

4. Conclusions

The Schiff base 4-chloro-2-(*N*-ethyliminomethyl)-phenol (HL) was prepared *in situ via* the condensation reaction of 5-chloro-salicylaldehyde and ethylamine and was isolated in the form of its Pd(II) complex, formulated as [Pd(4-chloro-2-(ethyliminomethyl)-phenolato-κ^2N,O)$_2$], **1**. The structure of complex **1** was determined by single-crystal X-ray crystallography, revealing tetrahedral square planar geometry of the palladium atom.

The biological potency of the resultant complex **1** was evaluated *in vitro* and *in silico*. *In vitro* studies include the evaluation of its antibacterial activity against a series of Gram(−) and Gram(+) bacteria and its interaction with DNA (CT and plasmid) and albumins (HSA and BSA). The study of the antibacterial activity revealed a moderate activity of the complex. The complex exhibits similar SA-fluorescence quenching ability and similar SA-binding affinity with similar Pd complexes, as evaluated by k_q and K constants, respectively. The SA-binding constants showed reversible binding of complex so that it can be transferred and released upon arrival at the potential targets. The complex may bind to CT DNA *via* intercalation with relatively high DNA-binding constant. The effect of the complex on pDNA seems to depend on the concentration of the complex revealing the formation of single-stranded closed-circles or a more compact form of supercoiled pDNA.

The results from the present molecular modeling simulations may provide useful complementary insights for the elucidation of the mechanism of action of the studied complex at a molecular level. Further *in silico* studies adopting various procedures, contributed in the understanding of the role of complex **1** in various diseases, suggesting a mode of action of this compound. *In silico* calculations can provide a molecular basis for the understanding of both the impairment of DNA by its binding with the studied complex and also the ability of this compound for transportation through blood serum albumin and possible interaction with other protein targets involved in various diseases.

Undertaken *in silico* approach could be informative in pointing out the mechanism of action of complex **1** in a molecular level. The results from these predictive tools contributed to better understanding of the biological activity of the compound, providing useful complementary insight into the elucidation of its mechanism of action at the molecular level and the interpretation of its biological activity in many diseases.

Abbreviations

ADMET	absorption distribution metabolism excretion and toxicity
admetSAR	ADMET structure-activity relationship
AR	androgen receptor
B. cereus	*Bacillus cereus* ATCC 11778
B. subtilis	*Bacillus subtilis* ATCC 6633
BS	binding site
BSA	bovine serum albumin
CBN	chlorobiocin
ccc	covalently closed circular
CLC-Pred	Cell Line Cytotoxicity Predictor
CNR1	Cannabinoid receptor 1
CT	calf-thymus
DIGEP-Pred	drug-induced gene expression profiles prediction
DMF	*N,N*-dimethylformamide
DMSO	dimethylsulfoxide
E. coli	*Escherichia coli* XL1
EB	ethidium bromide, 3,8-diamino-5-ethyl-6-phenyl-phenanthridinium bromide
E	estrogen receptor
ESI	electrospray ionization

H-b	hydrogen-bond
HL	4-chloro-2-(*N*-ethyliminomethyl)-phenol
H-ph	hydrophobic
HSA	human serum albumin
IBP	ibuprofen, 2-(4-isobutylphenyl)propionic acid
IC$_{50}$	Half-Minimal Inhibitory Concentration
K	SA-binding constant
K$_b$	DNA-binding constant
k$_q$	quenching constant
K$_{SV}$	Stern-Volmer constant
L$^-$	4-chloro-2-(ethyliminomethyl)-phenolato anion
LBD	Ligand-Binding Domain
LD$_{50}$	median lethal dose
MAPT	microtubule-associated protein tau
MBC	Minimal Bactericidal Concentration
NPS	naproxen, (*S*)-2-(6-methoxynaphthalen-2-yl)propanoic acid
oc	open circular
Pa	probability "to be active"
PASS	prediction of activity spectra for substances
PDB	Protein Data Bank
pDNA	plasmid **pBluescript SK**(+)
Pi	probability "to be inactive"
PPB	plasma protein binding
ProTox-II	prediction of toxicity-II
r	[compound]/[DNA] ratio or [compound]/[SA] ratio
r'	[DNA]/[compound] ratio
ROSC-Pred	rodent organ-specific carcinogenicity prediction
S. aureus	*Staphylococcus aureus* ATCC 29213
SA	serum albumin
saloH	salicylaldehyde
sh	shoulder
SMP	substrate/metabolite specificity prediction
SOMP	sites of metabolism prediction
X. campestris	*Xanthomonas campestris* ATCC 33013
X-saloH	substituted salicylaldehyde

Appendix A. Supplementary data

CCDC 1902990 contains the supplementary crystallographic data for this paper. These data can be obtained free of charge *via* www.ccdc.cam.ac.uk/conts/retrieving.html (or from the Cambridge Crystallographic Data Centre, 12 Union Road, Cambridge CB21EZ, UK; fax: (+44) 1223-336-033; or deposit@ccde.cam.ac.uk). Supplementary data associated with this article can be found, in the online version, at https://doi.org/10.1016/j.jinorgbio.2019.110792.

References

[1] M. Tanaka, H. Kataoka, S. Yano, H. Ohi, K. Kawamoto, T. Shibahara, T. Mizoshita, Y. Mori, S. Tanida, T. Kamiya, T. Joh, BMC Cancer 13 (2013) 237–246.

[2] B. Kaur, N. Kaur, S. Kumar, Coord. Chem. Rev. 358 (2018) 13–69.

[3] A. Trevisan, C. Marzano, P. Cristofori, M.B. Venturini, L. Giovagnini, D. Fregona, Arch. Toxicol. 76 (2002) 262–268.

[4] M. Fanelli, M. Formica, V. Fusi, L. Giorgi, M. Micheloni, P. Paoli, Coord. Chem. Rev. 310 (2016) 41–79.

[5] Z.D. Bugarcic, J. Bogojeski, R. van Eldik, Coord. Chem. Rev. 292 (2015) 91–106.

[6] A. Garoufis, S.K. Hadjikakou, N. Hadjiliadis, Coord. Chem. Rev. 253 (2009) 1384–1397.

[7] F. Shaheen, A. Badshah, M. Gielen, G. Croce, U. Florke, S. Ali, J. Organomet. Chem. 695 (2010) 315–322.

[8] M. Gaber, H.A. El-Ghamry, S.K. Fathalla, Spectrochim. Acta Part A 139 (2015) 396–404.

[9] S. Medici, M. Peana, V.M. Nurchi, J.I. Lachowicz, G. Crisponi, M.A. Zoroddu, Coord. Chem. Rev. 284 (2015) 329–350.

[10] W.A. Zoubi, Y.G. Ko, Appl. Organomet. Chem. 31 (2017) e3574.

[11] W.A. Zoubi, A.A.S. Al-Hamdani, M. Kaseem, Appl. Organomet. Chem. 30 (2016) 810–817.

[12] X. Liu, C. Manzur, N. Novoa, S. Celedon, D. Carrillo, J. Hamon, Coord. Chem. Revi. 357 (2018) 144–172.

[13] D. Gong, B. Wang, X. Jia, X. Zhang, Dalton Trans. 43 (2014) 4169–4178.

[14] D. Bandyopadhyay, M. Layek, M. Fleck, R. Saha, C. Rizzoli, Inorg. Chim. Acta 461 (2017) 174–182.

[15] M. Usman, F. Arjmand, M. Ahmad, M.S. Khan, I. Ahmad, S. Tabassum, Inorg. Chim. Acta 453 (2016) 193–201.

[16] R.K. Mohapatra, A.K. Sarangi, M. Azam, M.M. El-ajaily, M. Kudrat-E-Zahan, S.B. Patjoshi, D.C. Dash, J. Mol. Struct. 1179 (2019) 65–75.

[17] P. Rathelot, P. Vanelle, M. Gasquet, F. Delmas, M.P. Crozet, P. Timon-David, J. Maldonado, Eur. J. Med. Chem. 30 (1995) 503–508.

[18] Z. Hong, X. Zhang, T. Wu, C. Zheng, B. Luo, J. Tang, F. Huang, D. Yao, H. Bian, Polyhedron 159 (2019) 355–364.

[19] Z. Saedi, E. Hoveizi, M. Roushani, S. Massahi, M. Hadian, K. Salehi, J. Mol. Struct. 1176 (2019) 207–216.

[20] D. Sriram, P. Yogeeswari, N.S. Myneedu, V. Saraswat, Bioorg. Med. Chem. Lett. 16 (2006) 2127–2129.

[21] L. Zhou, C.C. Kwok, G. Cheng, H. Zhang, C.M. Che, Opt. Lett. 38 (2013) 2373–2375.

[22] S.A. Lee, G.R. You, Y.W. Choi, H.Y. Jo, A.R. Kim, I. Noh, S.J. Kim, Y. Kim, C. Kim, Dalton Trans. 43 (2014) 6650–6659.

[23] C.R. Nayar, R. Ravikumar, J. Coord. Chem. 67 (2014) 1–16.

[24] S.M. Borisov, R. Saf, R. Fischer, I. Klimant, Inorg. Chem. 52 (2013) 1206–1216.

[25] A.W. Jeevadason, K.K. Murugavel, M.A. Neelakantan, Renew. Sust. Energ. Rev. 36 (2014) 220–227.

[26] C.E. Satheesh, P.R. Kumar, P. Sharma, K. Lingaraju, B.S. Palakshamurthy, H.R. Naika, Inorg. Chim. Acta 442 (2016) 1–9.

[27] R.R. Coombs, M.K. Ringer, J.M. Blacquiere, J.C. Smith, J.S. Neilsen, Y. Uh, J.B. Gilbert, L.J. Leger, H. Zhang, A.M. Irving, S.L. Wheaton, C.M. Vogels, S.A. Westcott, A. Decken, F.J. Baerlocher, Trans. Met. Chem. 30 (2005) 411–418.

[28] V.P. Petrovic, M.N. Zivanovic, D. Simijonovic, J. Dorovic, Z.D. Petrovic, S.D. Markovic, RSC Adv. 5 (2015) 86274–86281.

[29] M. Khorshidifard, H.A. Rudbari, B. Askari, M. Sahihi, M.R. Farsani, F. Jalilian, G. Bruno, Polyhedron 95 (2015) 1–13.

[30] A. Kumar, M. Agarwal, A.K. Singh, Polyhedron 27 (2008) 485–492.

[31] S. Priyarega, D.S. Raja, S.G. Babu, R. Karvembu, T. Hashimoto, A. Endo, K. Natarajan, Polyhedron 34 (2012) 143–148.

[32] K. Sharma, M.K. Biyala, M. Swami, N. Fahmi, R.V. Singh, Russ. J. Coord. Chem. 35 (2009) 142–148.

[33] G. Garcia-Friaza, A. Fernandez-Botello, J.M. Perez, M.J. Prieto, V. Moreno, J. Inorg. Biochem. 100 (2006) 1368–1377.

[34] P. Kavitha, K.L. Reddy, Arab. J. Chem. 9 (2016) 640–648.

[35] K.A. Majorek, P.J. Porebski, A. Dayal, M.D. Zimmerman, K. Jablonska, A.J. Stewart, M. Chruszcz, W. Minor, Mol. Immunol. 52 (2012) 174–182.

[36] E.L. Gelamo, C.H.T.P. Silva, H. Imasato, M. Tabaka, Protein Structure and Molecular Enzymology 1594 (2002) 84–99.

[37] G. Fanali, A. di Masi, V. Trezza, M. Marino, M. Fasano, P. Ascenzi, Mol. Asp. Med. 33 (2012) 209–290.

[38] K. Yamasaki, V.T. Chuang, T. Maruyama, M. Otagiri, Biochim. Biophys. Acta 1830 (2013) 5435–5443.

[39] K. Gurova, Future Oncol. 5 (2009) 1685–1704.

[40] M. Gellert, K. Mizuuchi, M.H. O'Dea, H.A. Nash, Proc. Natl. Acad. Sci. U. S. A. 73 (1976) 3872–3876.

[41] L.L. Shen, D.T.W. Chu, Curr. Pharm. Des. 2 (1996) 195–208.

[42] A. Zianna, G.D. Geromichalos, A.G. Hatzidimitriou, E. Coutouli-Argyropoulou, M. Lalia-Kantouri, G. Psomas, J. Inorg. Biochem. 194 (2019) 85–96.

[43] M.F. Reichmann, S.A. Rice, C.A. Thomas, P. Doty, J. Am. Chem. Soc. 76 (1954) 3047–3053.

[44] J. Marmur, J. Mol. Biol. 3 (1961) 208–211.

[45] Bruker Analytical X-ray Systems, Inc, Apex2, Version 2 User Manual, M86-E01078, Madison, WI, (2006).

[46] Siemens Industrial Automation, Inc., SADABS: Area-Detector Absorption Correction, Madison, WI (1996).

[47] L. Palatinus, G. Chapuis, J. Appl. Crystallogr. 40 (2007) 786–790.

[48] P.W. Betteridge, J.R. Carruthers, R.I. Cooper, K. Prout, D.J. Watkin, J. Appl. Crystallogr. 36 (2003) 1487.

[49] D.J. Watkin, C.K. Prout, L.J. Pearce, CAMERON Program, Chemical Crystallographic Laboratory, Oxford University, UK, 1996.

[50] W.J. Geary, Coord. Chem. Rev. 7 (1971) 81–122.

[51] E. Frasson, C. Panattoni, L. Sacconi, Acta Crystallogr. 17 (1964) 85–89.

[52] D.C. Bradley, M.B. Hursthouse, I.F. Rendall, J. Chem. Soc. D: Chem. Commun. (1969) 672–673.

[53] H. Torayama, H. Asada, M. Fujiwara, T. Matsushita, Polyhedron 17 (1998) 3859–3874.

[54] J. Du Bois, C.T. Tomooka, J. Hong, E.M. Carreira, M.W. Day, Angew. Chem. Int. Ed. 36 (1997) 1645–1647.

[55] C. Li, R. Li, S. Zhang, Acta Crystallogr. Sect. E 66 (2010) m1122.

[56] C.J. Groombridge, L.F. Larkworthy, A. Marecaux, D.C. Povey, G.W. Smith, J. Mason, J. Chem. Soc. Dalton Trans. (1992) 3125–3131.

[57] Q. Huang, J. Guo, Y. Zhang, S. Zhang, Acta Crystallogr. Sect. E 68 (2012) m1047.

[58] T.C. Jones, T.N. Waters, B. Kaitner, B. Kamenar, Croat. Chem. Acta 59 (1986) 825–831.

[59] B. Kamenar, B. Kaitner, A. Stefanovic, T.N. Waters, Acta Crystallogr. Sect. C 46 (1990) 1627–1631.

[60] F. Chen, S. Zhang, J. Guo, Y. Zhang, C. Feng, Acta Crystallogr. Sect. E 67 (2011) m858.

[61] Q. Huang, S. Zhang, J. Guo, C. Feng, F. Tang, Acta Crystallogr. Sect. E 67 (2011) m1611.

[62] R. Knoch, H. Elias, H. Paulus, Inorg. Chem. 34 (1995) 4032–4040.

[63] R.J. Butcher, J.W. Overman, E. Sinn, J. Amer. Chem. Soc. 102 (1980) 3276–3278.

[64] E.N. Baker, G.R. Clark, D. Hall, T.N. Waters, J. Chem. Soc. A (1967) 251–257.
[65] G.R. Clark, D. Hall, T.N. Waters, J. Chem. Soc. A (1969) 2808–2813.
[66] C. Kao, H. Wei, Y. Liu, G. Lee, Y. Wang, C. Lee, J. Inorg. Biochem. 84 (2001) 171–178.
[67] E. Sinn, W.T. Robinson, J. Chem. Soc. Chem. Commun. (1972) 359–361.
[68] E. Sinn, Inorg. Chem. 15 (1976) 2698–2712.
[69] E. Sinn, Inorg. Chem. 15 (1976) 366–369.
[70] M. Dreher, H. Elias, H. Paulus, Zeit. Naturforsch. B: Chem. Sci. 42 (1987) 707–710.
[71] D.C. Bradley, M.B. Hursthouse, I.F. Rendall, J. Chem. Soc. Chem. Commun. (1970) 368.
[72] M. Sanz, T. Cuenca, M. Galakhov, A. Grassi, R.K.J. Bott, D.L. Hughes, S.J. Lancaster, M. Bochmann, Organometallics 23 (2004) 5324–5331.
[73] S. Pattanayak, K. Pramanik, N. Bag, P. Ghosh, A. Chakravorty, Polyhedron 16 (1997) 2951–2956.
[74] A. Dar, K. Moss, S.M. Cottrill, R.V. Parish, C.A. McAuliffe, R.G. Pritchard, B. Beagley, J. Sandbank, J. Chem. Soc. Dalton Trans. (1992) 1907–1913.
[75] P. Calamai, A. Guerri, L. Messori, P. Orioli, G.P. Speroni, Inorg. Chim. Acta 285 (1999) 309–312.
[76] R.J. Hill, C.E.F. Rickard, J. Inorg. Nucl. Chem. 40 (1978) 793–797.
[77] R.M. Silverstein, G.C. Bassler, G. Morvill, Spectrometric Identification of Organic Compounds, 6th ed., Wiley, New York, 1998.
[78] K. Nakamoto, Infrared and Raman Spectra of Inorganic and Coordination Compounds, Part B: Applications in Coordination, Organometallic, and Bioinorganic Chemistry, 6th ed., Wiley, New Jersey, 2009.
[79] A.B.P. Lever, Inorganic Electronic Spectroscopy, Elsevier, Amsterdam, 1984.
[80] L.P. Romm, A.A. Malkov, S.A. Lebedev, V.V. Levashova, T.M. Buslaeva, Russ. J. Phys. Chem. A 85 (2011) 248–253.
[81] B.M. Zeglis, V.C. Pierre, J.K. Barton, Chem. Commun. (2007) 4565–4576.
[82] Q. Zhang, J. Liu, H. Chao, G. Xue, L. Ji, J. Inorg. Biochem. 83 (2001) 49–55.
[83] A.M. Pyle, J.P. Rehmann, R. Meshoyrer, C.V. Kumar, N.J. Turro, J.K. Barton, J. Am. Chem. Soc. 111 (1989) 3051–3058.
[84] A. Wolfe, G. Shimer, T. Meehan, Biochemistry 26 (1987) 6392–6396.
[85] E. Sindhuja, R. Ramesh, N. Dharmaraj, Y. Liu, Inorg. Chim. Acta 416 (2014) 1–12.
[86] P. Kalaivani, C. Umadevi, R. Prabhakaran, F. Dallemer, P.S. Mohan, K. Natarajan, Polyhedron 80 (2014) 97–105.
[87] J.L. Garcia-Gimenez, M. Gonzalez-Alvarez, M. Liu-Gonzalez, B. Macias, J. Borras, G. Alzuet, J. Inorg. Biochem. 103 (2009) 923–934.
[88] S. Dhar, M. Nethaji, A.R. Chakravarty, J. Inorg. Biochem. 99 (2005) 805–812.
[89] G. Zhao, H. Lin, S. Zhu, H. Sun, Y. Chen, J. Inorg. Biochem. 70 (1998) 219–226.
[90] D.P. Heller, C.L. Greenstock, Biophys. Chem. 50 (1994) 305–312.
[91] N.P. Andreou, K. Dafnopoulos, C. Tortopidis, A.E. Koumbis, M. Koffa, G. Psomas, K.C. Fylaktakidou, J. Photochem. Photobiol. B Biol. 158 (2016) 30–38.
[92] D. Kovala-Demertzi, M.A. Demertzis, E. Filiou, A.A. Pantazaki, J.R. Miller, Y. Zheng, D.A. Kyriakidis, Biometals 16 (2003) 411–418.
[93] A.B. Ozcelik, S. Utku, F. Gumuş, A.C. Keskin, L. Acik, S. Yılmaz, A. Ozgungor, J. Enz. Inhib. Med Chem. 27 (2012) 413–418.
[94] A. Dimitrakopoulou, C. Dendrinou-Samara, A.A. Pantazaki, M. Alexiou, E. Nordlander, D.P. Kessissoglou, J. Inorg. Biochem. 102 (2008) 618–628.
[95] T. Afrati, A.A. Pantazaki, C. Dendrinou-Samara, C. Raptopoulou, A. Terzis, D.P. Kessissoglou, Dalton Trans. 39 (2010) 765–775.
[96] O. Antonoglou, K. Lafazanis, S. Mourdikoudis, G. Vourlias, T. Lialiaris, A. Pantazaki, C. Dendrinou-Samara, Mat. Sci. Eng. C 99 (2019) 264–274.
[97] X. He, D.C. Carter, Nature 358 (1992) 209–215.
[98] R.E. Olson, D.D. Christ, Ann. Rep. Med. Chem. 31 (1996) 327–336.
[99] C. Tan, J. Liu, H. Li, W. Zheng, S. Shi, L. Chen, L. Ji, J. Inorg. Biochem. 102 (2008) 347–358.
[100] I. Petitpas, T. Grune, A.A. Bhattacharya, S. Twine, M. East, S. Curry, J. Mol. Biol. 314 (2001) 955–960.
[101] J.R. Lakowicz, Principles of Fluorescence Spectroscopy, 3rd ed., Plenum Press, New York, 2006.
[102] L. Stella, A.L. Capodilupo, M. Bietti, Chem. Commun. (2008) 4744–4746.
[103] V. Rajendiran, R. Karthik, M. Palaniandavar, H. Stoeckli-Evans, V.S. Periasamy, M.A. Akbarsha, B.S. Srinag, H. Krishnamurthy, Inorg. Chem. 46 (2007) 8208–8221.
[104] S. Wu, W. Yuan, H. Wang, Q. Zhang, M. Liu, K. Yu, J. Inorg. Biochem. 102 (2008) 2026–2034.
[105] O.H. Laitinen, V.P. Hytonen, H.R. Nordlund, M.S. Kulomaa, Cell. Mol. Life Sci. 63 (2006) 2992–3017.
[106] S. Sugio, A. Kashima, S. Mochizuki, M. Noda, K. Kobayashi, Protein Eng. 12 (1999) 439–446.
[107] A. Bujacz, K. Zielinski, B. Sekula, Proteins 82 (2014) 2199–2208.
[108] I. Petitpas, C.E. Petersen, C.E. Ha, A.A. Bhattacharya, P.A. Zunszain, J. Ghuman, N.V. Bhagavan, S. Curry, Proc. Natl. Acad. Sci. U. S. A. 100 (2003) 6440–6445.
[109] J.A. Ali, A.P. Jackson, A.J. Howells, A. Maxwell, Biochemistry 32 (1993) 2717–2724.
[110] J.A. Ali, G. Orphanides, A. Maxwell, Biochemistry 34 (1995) 9801–9808.
[111] A.I. Mohamed, A. Shar, K.A. Reem, E. Usama, J. Enz. Inhib. Med. Chem. 28 (2013) 530–538.
[112] M. Brvar, A. Perdih, M. Renko, G. Anderluh, D. Turk, T. Solmajer, J. Med. Chem. 55 (2012) 6413–6426.
[113] Z. Niknami, A. Eslamifar, A. Emamirazavi, A. Ebrahimi, R. Shirkoohi, EXCLI J. 16 (2017) 1009–1017.
[114] B. Rayet, C. Gelinas, Oncogene 18 (1999) 6938–6947.
[115] T.M. Wise-Draper, R.A. Mintz-Cole, T.A. Morris, D.S. Simpson, K.A. Wickenheiser-Brokamp, M.A. Currier, T.P. Cripe, G.C. Grosveld, S.I. Wells, Cancer Res. 69 (2009) 1792–1799.
[116] L.M. Privette Vinnedge, S. Ho, K.A. Wickenheiser-Brokamp, S.I. Wells, PLoS One 7 (2012) e46985.
[117] J.J. Duan, J. Cai, Y.F. Guo, X.W. Bian, S.C. Yu, Int. J. Cancer 139 (2016) 965–975.
[118] M. Maj, G. Hoermann, S. Rasul, W. Base, L. Wagner, J. Attems, J. Diabetes Res. (2016) 1964634.
[119] I. Grundke-Iqbal, K. Iqbal, Y. Tung, Proc. Natl. Acad. Sci. U. S. A. 83 (1986) 4913–4917.
[120] C. Duyckaerts, B. Delatour, M. Potier, Acta Neuropathol. 118 (2009) 5–36.
[121] G. Velasco, S. Hernandez-Tiedra, D. Davila, M. Lorente, Progress in Neuro Psychopharmacology and Biological Psychiatry 64 (2016) 259–266.
[122] A.H. Benz, C. Renne, E. Maronde, M. Koch, U. Grabiec, S. Kallendrusch, B. Rengstl, S. Newrzela, S. Hartmann, M.L. Hansmann, F. Dehghani, PLoS One 8 (2013) e81675.
[123] B. Mukhopadhyay, K. Schuebel, P. Mukhopadhyay, R. Cinar, G. Godlewski, K. Xiong, K. Mackie, M. Lizak, Q. Yuan, D. Goldman, G. Kunos, Hepatology 61 (2015) 1615–1626.
[124] E.M. Messalli, F. Grauso, R. Luise, A. Angelini, R. Rossiello, Am. J. Obstet. Gynecol. 211 234 (2014) e1–e6.
[125] C.K. Jung, W.K. Kang, J.M. Park, H.J. Ahn, S.W. Kim, S.T. Oh, K.Y. Choi, Oncol. Lett. 5 (2013) 870–876.
[126] G. Velasco, C. Sanchez, M. Guzman, Nat. Rev. Cancer 12 (2012) 436–444.
[127] M.M. Caffarel, C. Andradas, E. Perez-Gomez, M. Guzman, C. Sanchez, Cancer Treat. Rev. 38 (2012) 911–918.
[128] S. Pisanti, P. Picardi, A. D'Alessandro, C. Laezza, M. Bifulco, Trends Pharmacol. Sci. 34 (2013) 273–282.